High Order Upwind Schemes for Multidimensional Magnetohydrodynamics

P. Londrillo
Osservatorio Astronomico, Bologna, Italy
and

L. Del Zanna
Dipartimento di Astronomia e Scienza dello Spazio, Firenze, Italy

ABSTRACT

A general method for constructing high order upwind schemes for multidimensional magnetohydrodynamics (MHD), having as a main built-in condition the divergence-free constraint $\nabla \cdot \mathbf{B} = 0$ for the magnetic field vector $\mathbf{B}$, is proposed. The suggested procedure is based on *consistency* arguments, by taking into account the specific operator structure of MHD equations with respect to the reference Euler equations of gas-dynamics. This approach leads in a natural way to a staggered representation of the $\mathbf{B}$ field numerical data where the divergence-free condition in the cell-averaged form, corresponding to second order accurate numerical derivatives, is exactly fulfilled. To extend this property to higher order schemes, we then give general prescriptions to satisfy a $(r+1)^{th}$ order accurate $\nabla \cdot \mathbf{B} = 0$ relation for any numerical $\mathbf{B}$ field having a r^{th} order interpolation accuracy. Consistency arguments lead also to a proper formulation of the upwind procedures needed to integrate the induction equations, assuring the exact conservation in time of the divergence-free condition and the related continuity properties for the $\mathbf{B}$ vector components. As an application, a third order code to simulate multidimensional MHD flows of astrophysical interest is developed using ENO-based reconstruction algorithms. Several test problems to illustrate and validate the proposed approach are finally presented.

Subject headings: methods: numerical– MHD

1. Introduction

Many astrophysical plasmas, such as stellar (or galactic) atmospheres and winds, accretion disks and jets, can be described by the set of compressible magnetohydrodynamic (MHD) equations with dissipative terms neglected, since kinetic effects of astrophysical plasmas are quite small on dominant macroscopic scales. In these physical regimes, dynamical effects give rise to complex time dependent flows where localized sharp modes like shocks and current sheets couple with distributed nonlinear waves. It is therefore a main challenge to computational astrophysics to take properly into account both dynamical components.

Centered finite differences or spectral schemes are well suited for smooth fields and can support discontinuities only by introducing *enough* viscous/resistive dissipation. In this way field discontinuities are represented with a poor resolution and artificial heating takes place. On the other hand, upwind schemes achieve shock-capturing and localized high resolution in a natural way. When discontinuous solutions are of main interest, second order (in time and space) schemes are usually adopted, since they reconcile resolution with efficiency and stability needs. But in the general case, when coherent sharp field structures are embedded in a turbulent background, second order accuracy is no longer the optimal one, since the (implicit) numerical viscosity is still to high to resolve properly small scales motions. There are then compelling computational and physical reasons to develop higher order upwind schemes for MHD flows.

In recent years progress has been made in extending Godunov-type schemes developed for the Euler system of gas-dynamics to MHD, with main emphasis on the wave characteristic structure. In Brio & Wu (1988), and Roe & Balsara (1996) the problem of non strict hyperbolicity of the MHD system has been addressed by introducing proper regularity factors to renormalize the eigenvectors and assure their linear independence. The related problem of constructing the Roe linearized matrix for MHD case, has also been solved (Cargo & Gallice 1997, Balsara 1998a). Based on these achievements, second order upwind codes using either Godunov's or Roe's method have then been constructed and tested, mainly for one-dimensional MHD problems (e.g. Ryu & Jones 1995, Zachary et al. 1994, Dai & Woodward 1994, Balsara 1998b).

Specific new problems and limitations have to be considered in going to higher order and multidimensional MHD case. Upwind schemes are usually constructed by first projecting fluid variables at each grid point on the space of characteristic variables. The decomposition procedure allows to achieve a better resolution since interacting discontinuities of fluid variables become uncoupled in the space of characteristic variables. This technique is usually adopted also in existing MHD codes, but there is no clear evidence that it can work even for higher order schemes (Barmin et al. 1996). Moreover, the computational cost to project field variables onto the MHD seven-component characteristic space may become prohibitive when moving to higher order and higher dimensional schemes. Therefore, as already experienced in the context of numerical gas-dynamics, a search for high order shock-capturing schemes where no characteristic decomposition is needed and where attention is shifted more to a *vanishing viscosity* entropy satisfying model equations, rather than on approximate Riemann solvers, appears to be more promising.

A second important issue in multidimensional MHD schemes comes from the need to satisfy the divergence-free condition of the magnetic field vector. This property is a crucial one for two main reasons (Balsara & Spicer 1999):

- the conservation form of MHD equations for energy and momenta is based on the implicit $\nabla \cdot \mathbf{B} = 0$ condition, and
- all the topological aspects of magnetic field lines which are relevant to critical MHD phenomena, like reconnection, heavily rely on this condition.

On the other hand, this specific property has no easy representation in a numerical framework, like 1-D Godunov-type schemes, designed to handle compressive modes and shocks. This longstanding problem has been addressed by many authors and several recipes have been proposed and experimented so far. Depending on the adopted methodology, these works can be broadly classified into three main categories:

1. Many MHD codes are constructed by simply extending to higher dimensions 1-D Riemann solvers using a directional splitting technique, as for the Euler system (Zachary et al. 1994, Ryu et al. 1995, Balsara 1998b, for second order Godunov-type schemes; Jiang & Wu 1999,

for 5^{th} order WENO scheme). In this approach the $\nabla \cdot \mathbf{B} = 0$ condition breaks down, of course, and some correction step has then to be applied. Following Brackbill & Barnes 1980, a cleaning procedure is usually carried out by solving a Poisson equation, which is equivalent to add a new (elliptic) equation to the original hyperbolic MHD system. As an empirical recipe, this method is by no means optimal and may lead to inconsistencies. In particular, the numerical derivatives appearing in Poisson equation have no clear relation with the upwind derivatives of the base MHD system and the boundary conditions become indeterminate for nontrivial boundary-value problems.

2. In the Powell (1994) approach it is first pointed out the formal difficulty of applying 1-D Riemann solvers to the multidimensional case, since the 1-D MHD mode eigenspace, having seven components, is not of full rank for the 2-D case, where an eight-component state vector is involved. Therefore, variations of magnetic field components appearing in the $\nabla \cdot \mathbf{B}$ operator cannot be represented by Riemann solvers based on the 1-D eigenspace. This undoubtedly correct premise led the author to propose a modification of the MHD equations by adding a "$\nabla \cdot \mathbf{B}$ mode", propagating with the local flow speed. In this way the hyperbolic character of the MHD system is surely retained, at the price of suppressing the divergence-free property. This approach appears to be highly questionable, of course, since important physical properties of the MHD equations, and especially magnetic field topologies, are clearly lost.

3. In the present work we have taken as a main starting point all those references attempting to design upwind schemes where a numerical divergence-free condition works as a build-in property (Evans & Hawley 1988, DeVore 1991, Stone & Norman 1992, Dai & Woodward 1998, Ryu et al. 1998, Balsara & Spicer 1999, among others). In all these works, the introduction of the magnetic vector potential or the equivalent conservative formulation of Stoke's theorem lead to represent magnetic field components at staggered collocation points, and a numerical $\nabla \cdot \mathbf{B} = 0$ relation follows as an algebraic identity. Moreover, when induction equations are properly formulated in terms of the staggered fields, conservation in time of the divergence-free property is also assured.

   In the cited works, however, some main questions are still left open. These are essentially related to a persisting *duality* between staggered magnetic components evolving in the induction equations and the same components, now collocated at node points (or cell centers) as other fluid variables, entering the Riemann solver procedures. Several recipes based on interpolation have been suggested to relate cell centered and staggered fields. However, as widely discussed in the Dai & Woodward (1998) paper, the cell centered field components do not preserve, in general, the original divergence-free property, unphysical magnetic monopoles still arise and their sizes seem to depend on the adopted interpolation schemes.

   A related question concerns how upwind fluxes in the induction equations have to be formulated, since 1-D Riemann solvers for density, momentum and energy equations have no straightforward extension to them, when staggering is adopted. Again, many different empirical solutions have been proposed, which hardly can be compared and evaluated as long as only qualitative numerical tests are at disposal.

In the present paper we propose some *general* answers to these questions, by showing that *consistency* arguments are sufficient to envisage the main rules to adapt upwind schemes designed for Euler equations to the MHD case. Consistency requires that the specific operator structure of the MHD system and the related magnetic field properties have to be preserved by discretized equations and upwind procedures. In this way, different schemes and their high order extensions can be designed, all assuring a numerical divergence-free condition as well as the related uniqueness and regularity of magnetic field lines. On the same ground, existing MHD codes and published numerical results can be evaluated on a more appropriate framework.

The plan of the paper is as follows. In Sect. 2 the general formulation to discretize Euler and MHD equations in conservation form is reviewed, with emphasis on the differences in space operator structures and on the related numerical representation. In Sect. 3, the kinematical properties of discontinu-

ous, divergence-free magnetic field are first analyzed to represent numerical data and then used to construct appropriate upwind flux formulas (or approximate Riemann solvers) for the MHD equations. The proposed formulation is then also compared to recently published schemes. In Sect. 4 a code for 2-D systems, based on third order ENO-type reconstruction procedures and on the simple Lax-Friedrichs flux upwinding, is presented. Sect. 5 is devoted to numerical test problems to add confidence and validation of the proposed approach and conclusive remarks are briefly given in Sect.6.

2. Euler versus MHD systems

To underline differences between the Euler and MHD systems relevant to numerical discretization, we first briefly review some of the main points characterizing upwind schemes for the Euler equations. As a general framework, we consider here the flux vector splitting (FVS) formalism (van Leer 1982, Chen & Lefloch 1995) and the high order reconstruction techniques based on polynomials (Shu 1997). For ease of presentation we treat only the 2-D case in cartesian geometry, being both the 3-D case and curvilinear geometries just straightforward extensions.

2.1. Upwind schemes for Euler equations

The equations of gas-dynamics in two spatial dimensions constitute a system of $m = 5$ conservation laws:

$$\partial_t \mathbf{u} + \partial_x[\mathbf{f}(\mathbf{u})] + \partial_y[\mathbf{g}(\mathbf{u})] = 0, \tag{1}$$

where $\mathbf{u} = [\rho, \mathbf{q}, e]^T$ is the state vector of conservative variables, and

$$\mathbf{f} = [q_x, v_x q_x + p, v_x q_y, v_x q_z, v_x(e+p)]^T,$$

$$\mathbf{g} = [q_y, v_y q_x, v_y q_y + p, v_y q_z, v_y(e+p)]^T,$$

are the corresponding flux vector functions. Here ρ is the mass density, $\mathbf{q} = \rho\mathbf{v}$ the momentum associated with the flow velocity $\mathbf{v}$, e the total energy per unit volume and $p = (\gamma - 1)[e - \mathbf{q}\cdot\mathbf{v}/2]$ the gas pressure for a $\gamma-$law equation of state.

A basic property of the Euler system is that each Jacobian matrix, $\mathbf{A}_x(\mathbf{u}) = \partial_{\mathbf{u}}\mathbf{f}(\mathbf{u})$ and $\mathbf{A}_y(\mathbf{u}) = \partial_{\mathbf{u}}\mathbf{g}(\mathbf{u})$, has a set of m real eigenvalues $\{\lambda^s(\mathbf{u})\}$ ($s = 1, 2, \ldots, m$), and a corresponding complete set of right $\{\mathbf{R}_s(\mathbf{u})\}$ and left $\{\mathbf{R}_s^{-1}(\mathbf{u})\}$ eigenvectors, at every point $\mathbf{u}$ (hyperbolicity properties). Physically relevant solutions to system (1) are selected by imposing the admissibility condition

$$\partial_t[\rho F(s)] + \nabla\cdot[\rho F(s)\mathbf{v}] \le 0, \tag{2}$$

where $F(s)$ is any smooth function of the specific entropy $s(p,\rho)$ (Harten et al. 1998).

Numerical schemes for system (1) use the following *consistency conditions* as general guidelines (Tadmor 1988):

- the conservation form, assuring that numerical solutions capture correctly weak solutions;
- the entropy inequality, to be preserved by the discretized entropy functions. Upwind schemes are then designed to have (implicit) numerical viscosity compatible with relation (2).

In the semi-discrete formulation, appropriate for higher $r > 2$ order schemes, space operators are approximated (for a fixed time t) on a $N_x \times N_y$ dimensional grid with node points $N_{j,k} \equiv (x_j, y_k)$, where $x_j = h_x j$ ($j = 0, 1, \ldots, N_x - 1$) and $y_k = h_y k$ ($k = 0, 1, \ldots, N_y - 1$); here h_x and h_y are the constant grid sizes along each direction. The point values formulation based on $\{\mathbf{u}_{j,k}\}$ data leads then to the conservative scheme

$$\frac{d\mathbf{u}_{j,k}(t)}{dt} = -\frac{1}{h_x}[\hat{\mathbf{f}}_{j+1/2,k} - \hat{\mathbf{f}}_{j-1/2,k}] - \frac{1}{h_y}[\hat{\mathbf{g}}_{j,k+1/2} - \hat{\mathbf{g}}_{j,k-1/2}], \tag{3}$$

where $\hat{\mathbf{f}}_{j+1/2,k}$ and $\hat{\mathbf{g}}_{j,k+1/2}$ denote the numerical flux-vector functions needed to approximate the corresponding flux derivatives to a given order r. A numerical approximation is then characterized essentially by the way $\hat{\mathbf{f}}_{j+1/2,k}$ and $\hat{\mathbf{g}}_{j,k+1/2}$ are evaluated for a given set of $\{\mathbf{u}_{j,k}(t)\}$ data. Time integration can then be performed by appropriate Runge-Kutta or equivalent stable discretization schemes (Shu & Osher 1988).

Modern higher order shock-capturing schemes generalize first order Godunov scheme by following two main steps (Harten et al. 1987):

1. a reconstruction phase to recover variable values at grid points where flux derivatives have to be computed;
2. an upwind phase, where the Godunov method for a scalar conservation law in one dimension is extended to the $m > 1$ components system in higher dimensions.

As far as item 1 is concerned, we remind here some basic points relevant to the following sections and to the actual code structure, to be presented in Sect. 4.

Any one-dimensional piecewise smooth function $w(x)$, defined by cell averaged data

$$\overline{w}_j = \frac{1}{h_x}\int_{x_{j-1/2}}^{x_{j+1/2}} w(x)dx,$$

can be approximated by uniform $(r-1)^{th}$ order piecewise polynomials $P_j(x;\overline{w})$, which must have the conservative property $\overline{P}_j = \overline{w}_j$. Likewise, a $w(x)$ function defined by grid-point data $\{w_j = w(x_j)\}$ can be approximated by interpolation polynomials $P_j(x;w)$ defined as $P_j(x_j;w) = w_j$. Here we denote with $R[x;\overline{w}]$ (or $R[x;w]$) the corresponding polynomials set $\{P_j\}$ to reconstruct $w(x)$ at any x point.

At points of discontinuity, $R[x;\cdot]$ has to satisfy definite non-oscillatory constraints, for accuracy and stability purposes. Standard references are provided by linear polynomials based on *minmod* limiters to preserve monotonicity of data (MUSCL scheme: van Leer 1979; TVD scheme: Harten 1983) or by higher $r > 2$ order polynomials based on ENO procedures (Harten et al. 1987, Shu & Osher 1989) having weaker (essentially non-oscillatory) monotonicity properties. Piecewise polynomials approximate the $w(x)$ function at any cell boundary point $x_{j+1/2}$ by a two-point left-right $(w^{(L)}, w^{(R)})$ value, where

$$[w^{(L)}]_{j+1/2} = P_j(x_{j+1/2}) = w(x^-_{j+1/2}) + O(h_x^r),$$

$$[w^{(R)}]_{j+1/2} = P_{j+1}(x_{j+1/2}) = w(x^+_{j+1/2}) + O(h_x^r),$$

for smooth functions. For $w(x)$ having a discontinuous k^{th} derivative in the $x_j < x < x_{j+1}$ range, with $k < r$, the accuracy order becomes $O(h_x^{k+1})$.

The reconstruction procedures can be extended to the 2-D functions in Eq. (1) by assuming that the scalar components $u(x,y)$ (and hence $f[\mathbf{u}(x,y)]$ and $g[\mathbf{u}(x,y)]$) are piecewise smooth along each coordinate. In this way, calling $C_{j,k}$ the 2-D cell centered at the node point $N_{j,k}$, the functions $u(x,y)$ can be reconstructed at the cell edges $(x_{j+1/2}, y_k)$ and $(x_j, y_{k+1/2})$ by using respectively the 1-D operators $R[x;u_k]$ and $R[y;u_j]$. The same functions may also be reconstructed at a cell corner $P_{j,k} \equiv (x_{j+1/2}, y_{k+1/2})$ by using the 2-D compound operators $R[x_{j+1/2}; R[y_{k+1/2}; u]]$. Actually, space discretization in Eq. (1) involves only 1-D reconstructions, one for each direction. In fact, $\hat{f}_{j+1/2,k}$ is defined at the point $x = x_{j+1/2}$, for fixed $y = y_k$, where the argument variables have the two-state $x-$wise reconstructed values $[u^{(L,)}, u^{(R,)}]_k$; likewise, $\hat{g}_{j,k+1/2}$ is defined at the point $y = y_{k+1/2}$, for fixed $x = x_j$, where the argument variables have the two-state $y-$wise reconstructed values $[u^{(,L)}, u^{(,R)}]_j$.

Let us now turn our attention to item 2. In the FVS formalism, to represent a flux variation, say in the x coordinate, the vector $\mathbf{f}(\mathbf{u})$ is decomposed as

$$\mathbf{f}(\mathbf{u}) = \frac{1}{2}[\mathbf{f}^{(+)} + \mathbf{f}^{(-)}], \quad \mathbf{f}^{(\pm)} = \mathbf{f}(\mathbf{u}) \pm \mathbf{D}_x(\tilde{\mathbf{u}})\cdot\mathbf{u},$$

for states $\mathbf{u}$ around a given reference (constant) state $\tilde{\mathbf{u}}$. The flux vectors $\mathbf{f}^{(\pm)}$ have Jacobian matrices $\mathbf{A}_x(\tilde{\mathbf{u}}) \pm \mathbf{D}_x(\tilde{\mathbf{u}})$ with only positive/negative eigenvalues. The matrix $\mathbf{D}_x$ is then required to be real (symmetrizable) and positive, $\mathbf{D}_x(\tilde{\mathbf{u}}) \geq |\mathbf{A}_x(\tilde{\mathbf{u}})|$, where

$$|\mathbf{A}_x(\tilde{\mathbf{u}})| = \sum_s [\mathbf{R}_s|\lambda_s|\mathbf{R}_s^{-1}]_{\tilde{\mathbf{u}}}\,.$$

For given $\mathbf{u}_1 = \mathbf{u}^{(L,)}, \mathbf{u}_2 = \mathbf{u}^{(R,)}$ reconstructed values at the point $x_{j+1/2}$ and for fixed k index, flux splitting allows to define the numerical flux

$$\mathbf{f}(\mathbf{u}_1,\mathbf{u}_2)_{j+1/2,k} =$$

$$\frac{1}{2}[\mathbf{f}(\mathbf{u}_1) + \mathbf{f}(\mathbf{u}_2) - \mathbf{D}_x(\tilde{\mathbf{u}})\cdot(\mathbf{u}_2 - \mathbf{u}_1)]_{j+1/2,k}, \quad (4)$$

which has *upwind properties*, namely it is a two-point vector function non-increasing in the first argument and non-decreasing in the second argument. The reference state $\tilde{\mathbf{u}}$ is given by the Roe average or by the simpler $\tilde{\mathbf{u}} = (\mathbf{u}_1 + \mathbf{u}_2)/2$ arithmetic average, in a way to assure consistency $\mathbf{f}(\mathbf{u},\mathbf{u}) = \mathbf{f}(\mathbf{u})$ and continuous dependence on data.

Standard references for the scheme in Eq. (4) are given by either the approximate Riemann solvers of Roe-type or of Godunov-type , where the corresponding matrix $\mathbf{D}_x$ has the formal property

$$\mathbf{D}_x(\tilde{\mathbf{u}}) = |\mathbf{A}_x(\tilde{\mathbf{u}})| + O(|\mathbf{u}^{(L,)} - \mathbf{u}^{(R,)}|)$$

entailing a minimum of numerical viscosity compatible with the entropy law. On the other hand, a maximum of numerical viscosity is achieved by the (global) Lax-Friedrichs (LF) flux, where the $\mathbf{D}_x$ matrix reduces to the simple diagonal form

$$\mathbf{D}_x(\tilde{\mathbf{u}}) = \alpha\mathbf{I}, \quad \alpha = max_{\tilde{\mathbf{u}}}[max_s|\lambda_s(\tilde{\mathbf{u}})|],$$

and in which Riemann characteristic informations are averaged out. Note that the flux formula Eq. (4)

can be interpreted either as an approximate Riemann solver based on local linearization, or as a discrete approximation of the associated viscosity model equation. In fact, a first order approximation of the flux splitting is the discretized representation of the viscous flux

$$\mathbf{f}_v(\mathbf{u}) = \mathbf{f}(\mathbf{u}) - h_x \mathbf{D}_x \cdot \partial_x \mathbf{u}, \tag{5}$$

which provides a link between the entropy condition and the numerical viscosity associated to the dissipation matrix $h_x \mathbf{D}_x$.

In 2-D problems, the semi-discrete formulation of Eq. (3) and the independence of the Jacobian matrices $(\mathbf{A}_x, \mathbf{A}_y)$, allow one to represent the numerical fluxes $\hat{\mathbf{f}}_{j+1/2,k}$ (for fixed y_k) and $\hat{\mathbf{g}}_{j,k+1/2}$ (for fixed x_j) through independent upwind procedures, constructed with the matrices $\mathbf{D}_x$ and $\mathbf{D}_y$, respectively. In this way, the flux formula for $\mathbf{g}$ is given by

$$\mathbf{g}(\mathbf{u}_1, \mathbf{u}_2)_{j,k+1/2} =$$

$$\frac{1}{2}[\mathbf{g}(\mathbf{u}_1) + \mathbf{g}(\mathbf{u}_2) - \mathbf{D}_y(\tilde{\mathbf{u}}) \cdot (\mathbf{u}_2 - \mathbf{u}_1)]_{j,k+1/2}, \tag{6}$$

where $\mathbf{u}_1 = \mathbf{u}^{(,L)}$ $\mathbf{u}_2 = \mathbf{u}^{(,R)}$, are the reconstructed values at $y = y_{k+1/2}$, for fixed $x = x_j$. The corresponding viscosity form of the numerical flux $\mathbf{g}$ is given by

$$\mathbf{g}_v(\mathbf{u}) = \mathbf{g}(\mathbf{u}) - h_y \mathbf{D}_y \cdot \partial_y \mathbf{u}. \tag{7}$$

The construction of upwind fluxes in Eqs. (4) and (6), based on the $\mathbf{A}_x$ matrix eigenspace at the point $(x_{j+1/2}, y_k)$ and on the $\mathbf{A}_y$ matrix eigenspace at the point $(x_j, y_{k+1/2})$, is usually referred to as a *directional splitting* setting. This procedure is consistent with the divergence form of space operators in Eq. (1) and implies that the space derivatives are obtained by summing the two flux differences computed both at the same time t. In the Strang-type formalism, which is widely adopted in the numerical astrophysics community, a splitting procedure is also applied to the time evolution operators, by constructing the updated solution of a 2-D problem as a sequel of independent 1-D problems, one for each direction, in turn. In the Euler system directional splitting or time splitting procedures give (formally) equivalent results, at least for second order schemes. In the MHD case, however, this formal equivalence is definitely lost, as it will be discussed in the following.

2.2. The two-dimensional MHD system

The set of MHD conservation laws cannot be considered as a simple extension of the Euler system, with just a higher number of state variables. Actually, while the conservation form, the entropy law and the general hyperbolic properties are maintained, some specific differences related to the structure of the space operators have to be considered.

In fact, the MHD system can be viewed as composed by two coupled subsystems, the first one containing space operators in the divergence form as in Eq. (1) evolving density energy and momenta, and the second one, specific to the magnetic field evolution, containing space operators in the *curl* form. In both subsystems the $\nabla \cdot \mathbf{B} = 0$ property of the vector magnetic field enters in a substantial way and has then to be considered as a new consistency condition for numerical discretization.

By specializing again to 2-D systems, the MHD equations are given by

$$\partial_t \mathbf{u} + \partial_x[\mathbf{f}(\mathbf{w})] + \partial_y[\mathbf{g}(\mathbf{w})] = 0, \tag{8}$$

for the six-component state vector $\mathbf{u} = [\rho, \mathbf{q}, e, B_z]^T$, coupled with the induction equations

$$-\partial_t B_x + \partial_y \Omega(\mathbf{w}) = 0, \quad \partial_t B_y + \partial_x \Omega(\mathbf{w}) = 0, \tag{9}$$

for the (poloidal) vector field $\mathbf{B} = [B_x, B_y]^T$. We denote the overall eight-component state vector as $\mathbf{w} = [\mathbf{u}, \mathbf{B}]^T$. The flux vectors in Eq. (8) are given by

$$\mathbf{f}(\mathbf{w}) = [q_x, F_{x,x}, F_{x,y}, F_{x,z}, E_x, G_{x,z}]^T,$$
$$\mathbf{g}(\mathbf{w}) = [q_y, F_{y,x}, F_{y,y}, F_{y,z}, E_y, G_{y,z}]^T,$$

where, for indexes $i, j = x, y, z$:

$$F_{i,j} = v_i q_j - B_i B_j + \Pi \delta_{i,j},$$
$$E_i = v_i(e + \Pi) - B_i(v_j B_j),$$
$$G_{i,j} = v_i B_j - v_j B_i,$$

in which the relations $F_{i,j} \equiv F_{j,i}$ and $G_{i,j} \equiv -G_{j,i}$ clearly hold. Here $\Pi = p + (B_i B_i)/2$ and $p = (\gamma - 1)[e - (q_i v_i)/2 - (B_i B_i)/2]$ are respectively the total and the gas pressures. The common flux function of Eqs. (9) is defined as $\Omega = G_{x,y} \equiv -G_{y,x} = v_x B_y - v_y B_x$.

For given $\mathbf{B}$ field, the subsystem (8) as an *Euler form*, with independent Jacobian matrices of full $m = 6$ rank, so that the upwinding procedures based

on directional splitting of the previous section can be extended. Differences arise, however, for the induction equations. In fact, subsystem (9) is generated by a *unique* flux function and has then only a one-dimensional eigenspace. This formal property is clearly related to the $\nabla \cdot \mathbf{B} = 0$ condition, as can be better evidenced by introducing a vector potential representation of the (poloidal) $\mathbf{B}$ components (here $A \equiv A_z$)

$$B_x = \partial_y A, \quad B_y = -\partial_x A, \tag{10}$$

For given smooth (B_x, B_y) fields, $A(x, y)$ always exists as a one-valued differentiable function. For discontinuous fields, Eq. (10) still holds in weak form, implying that $A(x, y)$ is at least (Lipschitz) continuous along each coordinate. On the other hand, for given $A(x, y, t)$, the system given by Eqs. (9) is fully equivalent to the one-component evolution equation

$$\partial_t A - \Omega(\mathbf{w}) = 0, \tag{11}$$

coupled with Eqs. (10).

In a formal setting, for given state variables $\mathbf{u}$, Eq. (11) is a Hamilton-Jacobi equation (Jin & Xin 1998), and Eqs. (9) represent the associated hyperbolic system. An important property of Eqs. (11) is that $A(x, y, t)$ is continuous at all times and only discontinuities in its first derivatives may develop. Therefore, field lines defined by the isocontours $A(x, y) =$ const are allowed to have *corners*, but not jumps.

The overall MHD system can then be viewed as a coupled system of a Hamilton-Jacobi equation and of a set of conservation laws in the Euler form. One consequence is that the Jacobian matrix $\mathbf{A}_x$ corresponding to the $[\mathbf{f}, \Omega]^T$ vector flux is only of $m = 7$ rank and can represent characteristic modes of variables $\mathbf{w}_x = [\mathbf{u}(x,), B_y(x,)]^T$, while the independent matrix $\mathbf{A}_y$, corresponding to the $[\mathbf{g}, -\Omega]^T$ vector flux, can represent variables $\mathbf{w}_y = [\mathbf{u}(, y), B_x(, y)]^T$. It is evident that the missing degrees of freedom $[B_x(x,), B_y(, y)]$ are not evolutionary and cannot have a characteristic-based representation.

A numerical schemes preserving these general properties must then be be characterized by the following points:

1. A numerical $\nabla \cdot \mathbf{B} = 0$ condition and its conservation in time imply that the induction equations (9) have to be discretized using a *unique* flux function $\Omega(\mathbf{w})$ located at common points. This entails necessarily a staggered collocation of the magnetic field scalar components.

2. A divergence-free magnetic field is fully equivalent to its representation via a numerical vector potential and likewise the evolution equations (9), discretized as in item 1, can always be integrated via the scalar Eq. (11).

3. Relevant to the reconstruction and upwind steps is that the magnetic field components are at least continuous along the respective longitudinal coordinates, while discontinuities, to be related to the MHD characteristic modes, can occur only along the respective orthogonal coordinates (see below).

3. $\nabla \cdot \mathbf{B} = 0$ preserving upwind schemes for MHD equations

In this section we concentrate on the correct collocation and reconstruction step for the numerical magnetic field data, and then on the upwind flux formulation for the induction equations, in order to preserve the peculiar features of the MHD system as outlined just above.

3.1. The reconstruction step

While for given data $\{u_{i,j}\}$ of $\mathbf{u}$ variables in Eq. (8) the reconstruction procedures follow the same lines as in the Euler system (3), for the field $\mathbf{B}$ it is necessary to take into account the $\nabla \cdot \mathbf{B} = 0$ condition as a new kinematical constraint. For general piecewise smooth fields this condition is expressed in integral form by

$$\int_{\partial C} B_n d\, l = 0 \tag{12}$$

for any cell C, where $B_n = \mathbf{B} \cdot \mathbf{n}$ and $\mathbf{n}$ is the unit vector normal to the boundary line ∂C. By first choosing a cartesian cell with sides $[2\epsilon, h_y]$, the following continuity condition for the $y-$averaged $\overline{B}_x(x)$ component at any point x comes out:

$$\overline{B}_x(x + \epsilon) - \overline{B}_x(x - \epsilon) = O(\epsilon).$$

The same argument leads to the continuity of the $x-$averaged $\overline{B}_y(y)$ field at any point y.

If Eq. (12) is then integrated over a computational cell $C_{j,k}$, one has

$$h_y[\overline{B}_x(x_{j+1/2}) - \overline{B}_x(x_{j-1/2})]_k +$$

$$h_x[\overline{B}_y(y_{k+1/2}) - \overline{B}_y(y_{k-1/2})]_j = 0, \tag{13}$$

where $[\overline{B}_x]_k$ is the y average on the vertical cell side centered on y_k and $[\overline{B}_y]_j$ the corresponding x average over the horizontal cell side centered on x_j.

Continuity conditions and Eq. (13) are thus the main ingredients to construct at any point a divergence-free numerical field. In particular, the continuity condition $\overline{B}_x(x^+) = \overline{B}_x(x^-)$ allows one to locate the $[\overline{B}_x(x)]_k$ field at cell boundary points $\{x_{j+1/2}\}$, where all the other variables $[\mathbf{w}_x(x_{j+1/2})]_k$ are represented by reconstructed two-state (left-right) values. This property can be expressed in a formal way by setting $[\overline{B}_x^{(L,)}]_{j+1/2,k} = [\overline{B}_x^{(R,)}]_{j+1/2,k}$. Correspondingly, $\overline{B}_y(y)$ can be located at cell boundary points $\{y_{k+1/2}\}$ and point values can be interpreted as $[\overline{B}_y^{(,L)}]_{k+1/2} = [\overline{B}_y^{(,R)}]_{k+1/2}$.

The reconstruction step for the (B_x, B_y) fields along the respective transverse coordinates leads to the point values

$$[B_x(y)]_{j+1/2} = R[y; \overline{B}_x], \quad [B_y(x)]_{k+1/2} = R[x; \overline{B}_y],$$

which have relevance for upwind computations. In fact, at the $y_{k+1/2}$ point, $B_x(y_{k+1/2}) = [B_x^{(,R)}, B_x^{(,L)}]$ is a two-state variable, and can have only a transverse discontinuity line with a $\delta_y B_x = [B_x^{(,R)} - B_x^{(,L)}]$ jump. Similar arguments apply to the reconstructed values $B_y(x_{j+1/2}) = [B_y^{(R,)}, B_y^{(L,)}]$ at the $x = x_{j+1/2}$ boundary point, allowing only for a transverse discontinuity $\delta_x B_y = [B_y^{(R,)} - B_y^{(L,)}]$.

As already noticed by Evans & Hawley (1988), a main property related to condition (13) is that the numerical data $\{\overline{B}_x, \overline{B}_y\}$ allow one to construct a unique (continuous) numerical potential $A(x_{j+1/2}, y_{k+1/2})$, located at the cell corners $P_{j,k}$. It is evident that also the reverse condition holds true, by first introducing a numerical continuous function $A(x_{j+1/2}, y_{k+1/2})$ and then defining the averaged magnetic field components through Eqs. (10):

$$[\overline{B}_x(x_{j+1/2})]_k = \frac{1}{h_y}[\Delta_y A(x_{j+1/2})]_k,$$

$$[\overline{B}_y(y_{k+1/2})]_j = -\frac{1}{h_x}[\Delta_x A(y_{k+1/2})]_j, \qquad (14)$$

where (Δ_x, Δ_y) denote the usual (undivided) centered finite differences on the first and second coordinate index, respectively. In this way the divergence-free condition, Eq. (13), is identically satisfied by the commutativity of the Δ_x and Δ_y linear operators, whereas the continuity conditions follow from the continuity of $A(x, y)$. These arguments show, in particular, that the staggered collocation for $\{\overline{B}_x, \overline{B}_y\}$ data is by no means a numerical trick but arises in a consistent way from Eq. (13) or Eqs. (14).

Equation (13) gives the cell average of the $\nabla\cdot\mathbf{B} = 0$ condition, and thus it is an exact law for second order accurate schemes since $B_x = \overline{B}_x + O(h_y^2)$ at any point $(x_{j+1/2}, y_k)$ and $B_y = \overline{B}_y + O(h_x^2)$ at the corresponding staggered point. Now, if higher order approximation of point-valued B_x and B_y fields were recovered using independent reconstruction steps based on $\overline{B}_x$ and $\overline{B}_y$ data, a numerical $\nabla\cdot\mathbf{B}$ of any size could arise, in general, since 1-D reconstruction operators do not commute. To overcome this main difficulty, a different strategy has to be adopted, by first reconstructing accurate first derivatives based on the vector potential representation and having a numerical $\nabla\cdot\mathbf{B} = 0$ relation as a build-in property. As an illustration, in the following we consider third order interpolations, but extensions to higher order can be easily pursued.

We first notice that cell averaged $\overline{w}_j$ and point values w_j data of a given $w(x)$ function are related by $\overline{w}_j = w_j + \gamma_1 \mathcal{D}_x^{(2)}(w)_j + O(h^3)$, where $\gamma_1 = 1/24$ and $\mathcal{D}_x^{(2)}$ denotes a nonoscillatory numerical second derivative along the x coordinate. To the same accuracy, the inverse relation $w_j = \overline{w}_j - \gamma_1 \mathcal{D}_x^{(2)}(\overline{w})_j$ approximates point values using averaged data. This algorithm, now applied to the values $w_{j+1/2}$ at cell interfaces, $\hat{w}_{j+1/2} = [w - \gamma_1 \mathcal{D}_x^{(2)}(w)]_{j+1/2}$, gives the numerical $\hat{w}(x)$ primitive function whose two-point difference $[\Delta_x \hat{w}]_j/h_x$ constitutes a third order approximation of the $\partial_x w(x)$ first derivative at x_j. Let then apply this recostruction step to approximate the primitive $\hat{A}$ of the magnetic potential $A(x_{j+1/2}, y_{k+1/2})$. In the 2-D (x, y) plane we have

$$[\hat{A}]_{j+1/2,k+1/2} = [A - \gamma_1(\mathcal{D}_x^{(2)} + \mathcal{D}_y^{(2)})A]_{j+1/2,k+1/2},$$

and the numerical magnetic field components are

$$[\hat{B}_x]_{j+1/2,k} = \frac{1}{h_y}[\Delta_y \hat{A}]_{j+1/2,k},$$

$$[\hat{B}_y]_{j,k+1/2} = -\frac{1}{h_x}[\Delta_x \hat{A}]_{j,k+1/2}. \qquad (15)$$

By definition, the difference $[\Delta_x \hat{B}_x]/h_x$ gives a third order approximation of the $\partial_x B_x$ first derivative at the node (x_j, y_k) point, and $[\Delta_y \hat{B}_y]/h_y$ gives the corresponding approximation of the $\partial_y B_y$ derivative with the same accuracy and at the same point. We notice that no left or right derivatives are defined along

the longitudinal coordinates, thus these numerical approximations are unique. Moreover, one easily verifies that $\nabla \cdot \mathbf{B} = 0$, now in the point-valued form, is exactly fulfilled due to the commutativity of the $\Delta_x \Delta_y$ operator. The key point here is that to higher orders only the primitives $[\hat{B}_x(x,), \hat{B}_y(,y)]$ can be reconstructed directly using a common magnetic potential function $\hat{A}(x,y)$, but *not* the (B_x, B_y) functions themselves (those entering the fluxes, where divergence-free fields are actually needed). To achieve this, one needs a further computational step, that is to solve the (now implicit) relations

$$[B_x - \gamma_1 \mathcal{D}_x^{(2)} B_x]_{j+1/2,k} = [\hat{B}_x]_{j+1/2,k},$$

$$[B_y - \gamma_1 \mathcal{D}_y^{(2)} B_y]_{j,k+1/2} = [\hat{B}_y]_{j,k+1/2}, \qquad (16)$$

where on the left hand sides appear the primitives, and hence the derivatives, defined in terms of the (unknown) field point values, while on the right hand sides are the source terms $(\hat{B}_x, \hat{B}_y)$, given by Eqs. (15). The numerical fields (B_x, B_y) defined by these equations and the corresponding (longitudinal) derivatives are third order approximations but satisfy the divergence-free condition exactly. In practice one can solve Eqs. (16) by some explicit iterative algorithm, since each operator $(1 - \gamma_1 \mathcal{D}^{(2)})$ is clearly invertible and a fourth order accurate, at least, $\nabla \cdot \mathbf{B} = O(h_x^4, h_y^4)$ condition can then be easily satisfied (see Sect. 4).

This completes the main proof for the reconstruction step, needed to represent magnetic field point values in the momentum and energy equations, where longitudinal derivatives and hence a $\nabla \cdot \mathbf{B} = 0$ condition has to be satisfied to avoid numerical monopoles. Moreover, for given $[B_x]_{j+1/2,k}$ and $[B_y]_{j,k+1/2}$ data it is possible to get interpolated values at other collocation points, where these field components act as independent variables and no divergence-free condition is then required.

3.2. The upwind procedures

Let us now consider the first set of MHD equations (8) discretized as in Eq. (3):

$$\frac{d\mathbf{u}_{j,k}(t)}{dt} =$$

$$-\frac{1}{h_x}[\hat{\mathbf{f}}_{j+1/2,k} - \hat{\mathbf{f}}_{j-1/2,k}] - \frac{1}{h_y}[\hat{\mathbf{g}}_{j,k+1/2} - \hat{\mathbf{g}}_{j,k-1/2}], \qquad (17)$$

where now the flux functions $[\mathbf{f}(\mathbf{w}), \mathbf{g}(\mathbf{w})]$ depend on the eight-component vector $\mathbf{w} = [\mathbf{u}, \mathbf{B}]$. The upwind flux based on the $\mathbf{A}_x$ characteristic eigenspace has the form (consult Eq. (4)):

$$[\mathbf{f}(\mathbf{w}_x, B_x)]_{j+1/2,k} = \frac{1}{2}[\mathbf{f}(\mathbf{w}_x^{(R,)}, B_x) + \mathbf{f}(\mathbf{w}_x^{(L,)}, B_x)$$

$$-\mathbf{D}_x^{(1-6)}(\tilde{\mathbf{w}}) \cdot (\mathbf{w}_x^{(R,)} - \mathbf{w}_x^{(L,)})]_{j+1/2,k} \qquad (18)$$

where now upwind properties involve only the variables $\mathbf{w}_x = [\mathbf{u}, B_y]$. In the same way, the upwind flux based on the $\mathbf{A}_y$ characteristic eigenspace has the form (consult Eq. (6)):

$$[\mathbf{g}(\mathbf{w}_y, B_y)]_{j,k+1/2} = \frac{1}{2}[\mathbf{g}(\mathbf{w}_y^{(,R)}, B_y) + \mathbf{g}(\mathbf{w}_y^{(,L)}, B_y)$$

$$-\mathbf{D}_y^{(1-6)}(\tilde{\mathbf{w}}) \cdot (\mathbf{w}_y^{(,R)} - \mathbf{w}_y^{(,L)})]_{j,k+1/2}, \qquad (19)$$

where this time the upwind properties involve only the variables $\mathbf{w}_y = [\mathbf{u}, B_x]$.

To second order approximation, the numerical flux needed to compute space derivatives in Eq. (17) are given by the flux values of Eqs. (18,19), whose arguments $\mathbf{w}_x$ and $\mathbf{w}_y$ are second order interpolated variables. In particular $B_x = \overline{B}_x$) in the $\mathbf{f}(\mathbf{w}_x, B_x)$ flux and $B_y = \overline{B}_y$ in the $\mathbf{g}(\mathbf{w}_y, B_y)$ flux.

On the other hand, in classical second order schemes for the Euler equations the numerical flux $\hat{\mathbf{f}}$ is expressed using cell centered variables as

$$\hat{\mathbf{f}}_{j+1/2,k} = \frac{1}{2}[\mathbf{f}(\mathbf{w}_{j+1,k}) + \mathbf{f}(\mathbf{w}_{j,k})]$$

$$-\frac{1}{2}[\mathbf{D}_x^{(1-6)}(\tilde{\mathbf{w}}) \cdot (\mathbf{w}_x^{(R,)} - \mathbf{w}_x^{(L,)})]_{j+1/2,k}$$

and in a similar way for the $\mathbf{g}$ flux. However, this flux representation cannot be extended to the MHD case since cell centered (B_x, B_y) fields are not related by a divergence-free condition. The same remark applies to higher $r > 2$ order schemes where the numerical flux reconstruction is based on cell centered values (Shu & Osher 1989).

A second consequence of MHD structure in the evolution equations (17) is that the $\mathbf{u}$ state vector has to be integrated in time by *summing flux derivatives evaluated at the same time t*, when the implicit $\nabla \cdot \mathbf{B} = 0$ condition holds. In those schemes where time integration is performed by a Strang-type splitting procedure, flux derivatives and hence terms containing $\partial_x B_x$ and $\partial_y B_y$ are necessarily summed at

different time steps and the required $\partial_x B_x + \partial_y B_y$ cancellation never occurs.

To summarize, higher order upwind schemes developed for Euler equations can be extended to the MHD sub-system (17), with the proviso

1. flux derivatives have to be computed using flux values and hence **B** field data *directly* collocated at staggered (i.e. cell boundary centered) points and not at the cell centered points and,

2. the same derivatives along the two directions have to be computed *at the same time*, thus avoiding time-splitting techniques.

As already anticipated, the second set of MHD equations, given by the induction equations (9) for the magnetic poloidal field components, needs a particular treatment. In the proper, divergence-free preserving discretized form, these equations are given by

$$\frac{d}{dt}[\overline{B}_y(t)]_{j,k+1/2} = -\frac{1}{h_x}[\Delta_x \Omega(\mathbf{w}_P)],$$

$$\frac{d}{dt}[\overline{B}_x(t)]_{j+1/2,k} = \frac{1}{h_y}[\Delta_y \Omega(\mathbf{w}_P)], \qquad (20)$$

where now $\mathbf{w} = [v_x, v_y, B_x, B_y]^T$ denotes only the variables which are arguments of Ω. In a fully equivalent form using the vector potential representation, one has

$$\frac{d}{dt}[A(t)]_P = \Omega(\mathbf{w}_P), \qquad (21)$$

to be coupled with Eqs. (14). In both formulations a common flux function $\Omega(\mathbf{w})$, located at the cell corner point $P = [x_{j+1/2}, y_{k+1/2}]$, has to be evaluated.

In order to single out a consistent numerical flux function in Eq. (21), one has to take into account that $\Omega(\mathbf{w}_P)$ is now a four-state function

$$\Omega^{(a,b)} = \Omega[\mathbf{w}^{(a,b)}], \quad a, b = R, L,$$

and upwind rules involve necessarily *both* $\mathbf{A}_x(\tilde{\mathbf{w}})$ and $\mathbf{A}_y(\tilde{\mathbf{w}})$ matrix eigenspaces evaluated at a common reference state $[\tilde{\mathbf{w}}]_P$. To construct a proper 2-D Riemann flux formula, we first consider the two limiting cases in which a propagating discontinuity may be described by a 1-D Riemann flux formula.

1. For a discontinuity front perpendicular to the x direction, where $\mathbf{w}^{(,L)} = \mathbf{w}^{(,R)}$, one has

$$[\Omega_x(y)]_{j+1/2} = \frac{1}{2}[\Omega(\mathbf{w}^{(R,)}) + \Omega(\mathbf{w}^{(L,)}) - \mathbf{D}_x^{(7)}(\tilde{\mathbf{w}}) \cdot \delta_x \mathbf{w}_x](y)_{j+1/2}, \qquad (22)$$

where $\mathbf{D}_x^{(7)}$ denotes the seventh row vector component of $\mathbf{D}_x$ matrix and $\delta_x \mathbf{w}_x = (\mathbf{w}_x^{(R,)} - \mathbf{w}_x^{(L,)})$. The flux in Eq. (22) is extended to the range $y_k \le y \le y_{k+1}$ where the variables $\mathbf{w}^{(a,)}(y)$, $a = L, R$ are continuous. We remind here that the upwind formula (22) can be derived from the flux splitting introduced in Sect. 2.1, in the form

$$\Omega^{(\pm,)} = \Omega(\mathbf{w}) \pm \mathbf{D}_x^{(7)}(\tilde{\mathbf{w}}) \cdot \mathbf{w}_x, \qquad (23)$$

which is equivalent to a local linearization of the $\Omega(\mathbf{w}(x))$ flux around the $x = x_{j+1/2}$ point.

2. For a discontinuity front perpendicular to the y direction, where now $\mathbf{w}^{(L,)} = \mathbf{w}^{(R,)}$ the approximate Riemann solver reduces to

$$[\Omega_y(x)]_{k+1/2} = \frac{1}{2}[\Omega(\mathbf{w}^{(,R)}) + \Omega(\mathbf{w}^{(,L)}) + \mathbf{D}_y^{(7)}(\tilde{\mathbf{w}}) \cdot \delta_y \mathbf{w}_y](x)_{k+1/2}, \qquad (24)$$

where $\mathbf{D}_y^{(7)}$ denotes the seventh row vector component of the $\mathbf{D}_y$ matrix and $\delta_y \mathbf{w}_y = (\mathbf{w}_y^{(,R)} - \mathbf{w}_y^{(,L)})$. The x range involved is now $x_j \le x \le x_{j+1}$ where the variables $\mathbf{w}^{(,b)}(x)$, $b = L, R$ are continuous. Again, the upwind formula (24) may be derived from the splitting

$$\Omega^{(,\pm)} = \Omega(\mathbf{w}) \mp \mathbf{D}_y^{(7)}(\tilde{\mathbf{w}}) \cdot \mathbf{w}_y. \qquad (25)$$

which represents a local linearization around the $y = y_{k+1/2}$ point.

In the general case where a discontinuity front crosses the computational cell centered on P, an approximate Riemann solver can be obtained by introducing a 2-D flux splitting. For that purpose, we decompose each $\Omega^{(\pm,)}$ components in Eq. (23) along the y direction, with the requirement to have the same form of the symmetric decomposition of the $\Omega^{(\pm,)}$ components in Eq. (23) along the x direction. This compound flux splitting, when interpreted as an approximate Riemann solver with local linearization (thus implying to neglect $O(\delta_x \mathbf{w}_x \delta_y \mathbf{w}_y)$ terms), results in the four-state flux formula

$$\Omega(\mathbf{w}_P) = \frac{1}{4}[\Omega(\mathbf{w}^{(R,R)}) + \Omega(\mathbf{w}^{(R,L)}) + \Omega(\mathbf{w}^{(L,R)}) + \Omega(\mathbf{w}^{(L,L)})]_P$$

$$-\frac{1}{2}[\mathbf{D}_x^{(7)}(\tilde{\tilde{\mathbf{w}}})\cdot\delta_x\tilde{\mathbf{w}}_x-\mathbf{D}_y^{(7)}(\tilde{\tilde{\mathbf{w}}})\cdot\delta_y\tilde{\mathbf{w}}_y]_P, \qquad (26)$$

where $(a, b = R, L)$:

$$\tilde{\mathbf{w}}_x^{(a,)}=\frac{1}{2}(\mathbf{w}_x^{(a,R)}+\mathbf{w}_x^{(a,L)}),$$

$$\tilde{\mathbf{w}}_y^{(,b)}=\frac{1}{2}(\mathbf{w}_y^{(R,b)}+\mathbf{w}_y^{(L,b)}),$$

and $\tilde{\tilde{\mathbf{w}}}=(\mathbf{w}^{(R,R)}+\mathbf{w}^{(R,L)}+\mathbf{w}^{(L,R)}+\mathbf{w}^{(L,L)})/4$. The $\Omega(\mathbf{w})$ numerical flux given in Eq. (26) has now all the desired formal upwind properties both along the x and y directions, and reduces correctly to the 1-D limiting cases Eq. (22) and Eq. (24). The composition rule used here cannot be interpreted as a simple arithmetic average of independent 1-D Riemann solvers. In fact, for a discontinuity front with arbitrary slope angle around P, the 1-D flux formula, say Eq. (22), still applies and gives the upwind contribution along the x characteristic modes. Near the $y = y_{k+1/2}$ point, $\Omega_x^{(,b)}$ $(b = L, R)$ is now a two-state flux function and upwinding has to be completed by taking into account also the $-\mathbf{A}_y$ characteristic modes along the orthogonal y direction. By applying then 1-D flux upwinding as in Eq. (24) to the flux $\Omega(\mathbf{w}) = \Omega_x(\mathbf{w})$ and by discarding quadratic terms, one recovers Eq. (26). This composition procedure taken in reverse order, starting now from Eq. (24), yields an identical result under the essential assumption of linearization.

Finally, it is worth noticing that the viscous (resistive) model equation for the numerical flux function Ω, consistent with Eq. (26), has the form

$$\Omega_v(\mathbf{w})=\Omega(\mathbf{w})-\frac{1}{2}[h_x\mathbf{D}_x(\mathbf{w})\cdot\partial_x\mathbf{w}_x-h_y\mathbf{D}_y(\mathbf{w})\cdot\partial_y\mathbf{w}_y],$$

showing how the dissipative term generalizes the classical $\eta\mathbf{J} = \eta\nabla\times\mathbf{B}$ term in Ohm's law of resistive plasmas.

Having now completed the construction of the $\Omega(\mathbf{w})$ upwind flux for the induction equations, it is possible to design the overall numerical procedure to integrate the MHD system. We summarize here the main computational steps:

1. At each stage of the Runge-Kutta cycle, for given $[\mathbf{u}, A](t)$ data at time t, the averaged $[\overline{B}_x, \overline{B}_y]$ staggered fields are evaluated first by Eqs. (14).

2. Using then the $(\mathbf{u}, \overline{B}_x, \overline{B}_y)^T$ data, all variables $(\mathbf{u}, B_x, B_y)^T$ needed to compute the fluxes defined in Eqs. (18) are reconstructed at each cell boundary point $(x_{j+1/2}, y_k)$ and conservative x-derivatives of the $\mathbf{f}$ flux can then be evaluated.

3. The complementary procedure, now to reconstruct all variables $(\mathbf{u}, B_x, B_y)^T$ for the fluxes defined in Eqs. (19) at each $(x_j, y_{k+1/2})$ point, gives the conservative y-derivatives of the $\mathbf{g}$ flux.

4. A final reconstruction to the $(x_{j+1/2}, y_{k+1/2})$ corner point is needed to compute the $\Omega(\mathbf{w})$ numerical flux in Eq. (26). This allows to integrate in time the vector magnetic potential $A(t)$ by Eq. (21).

The explicit representation of a divergence-free magnetic field via a vector potential has, among others, the advantage of an easy extension to three-dimensional configurations. In fact, in this case one has to discretize the constitutive relations

$$\mathbf{B}=\nabla\times\mathbf{A}, \quad \mathbf{B}=[B_x, B_y, B_z]^T$$

in weak form to generalize Eqs. (14). The A_i, $i = x, y, z$ components and the corresponding flux functions $\Omega_i = [\mathbf{v}\times\mathbf{B}]_i$ are now located at the 3-D cell *edge* points P_i, each centered along the corresponding i^{th} coordinate but staggered with respect to the remaining two directions. The evolution equation Eq. (21) readily generalizes to

$$\frac{d[A_i(t)]_{P_i}}{dt}=\Omega_i(\mathbf{w}_{P_i})$$

and the consistency arguments introduced in $2D$ case can be applied to define the composition rules for each $\Omega_i = \Omega_i(\mathbf{w})$ scalar function since only two upwind directions, in turn, are now involved (*i.e.* each Ω_i involves a $2D$ Riemann solver).

3.3. Comments and discussion

Some remarks are due in order to underline differences and analogies with other proposed MHD schemes, in particular with those presented by Dai & Woodward (1998) (DW), by Ryu et al. (1998) (RY) and by Balsara & Spicer (1999) (BS), all claiming to have "divergence-free preserving properties". These works are based on second order either Godunov or Roe-type schemes and a staggered discretization for the induction equation of the form of our Eqs. (20) is used.

At a second order level the averaged variables $[\overline{B}_x]_{j+1/2,k}$ and $[\overline{B}_y]_{j,k+1/2}$ can be interpreted as

point valued variables at the same cell boundary points (which we label hereafter as (b_x, b_y) fields, to conform to the DW and RY notation). In Sect. 3 we have shown that these staggered, divergence-free variables, when used in momentum and energy equations avoid the effects of numerical monopoles. On the contrary, in all the cited works, while evolving in time the staggered (b_x, b_y) magnetic field, still interpolation and upwinding procedures are based on cell centered $(B_x, B_y)_{j,k}$ variables and unwanted compressive $\nabla \cdot \mathbf{B}$ terms then necessarily set up. Moreover, this "duality" in the magnetic field representation is considered to be unavoidable in the Godunov-type Riemann solvers formalism. For that reason, in the DW and BS papers in particular, much attention has been devoted to compare the different results produced by schemes advancing in time only the (b_x, b_y) staggered variables, where (B_x, B_y) work as interpolated variables, and schemes where *also* the (B_x, B_y) cell centered components are (independently) evolved (as for standard Godunov procedures for Euler equations). Conclusions are mainly drawn at a qualitative level, and only in the DW paper some numerical results on the $\nabla \cdot \mathbf{B}$ variable constructed with the (B_x, B_y) data are presented, showing the onset of significant, even of $O(1)$ size, residuals.

In the present approach, we have demonstrated by analytical arguments that the compressive components arise either in cases where cell centered fields are evolved in time or they are simply given by interpolation. In fact, at the leading second order interpolation used in the cited papers,

$$[B_x]_{j,k} = \frac{1}{2}([b_x]_{j+1/2,k} + [b_x]_{j-1/2,k}),$$

$$[B_y]_{j,k} = \frac{1}{2}([b_y]_{j,k+1/2} + [b_y]_{j,k-1/2}),$$

one gets a $O(h^2)$ (for smooth fields) residual when the $\nabla \cdot \mathbf{B}$ variable is evaluated by centered first derivatives. This compressive component associated to the (B_x, B_y) fields cannot be considered to be small (of the same order of the truncation error), since it is easy to show that even for higher order ($r > 2$) interpolation the leading $\nabla \cdot \mathbf{B} = O(h^2)$ term never cancels out.

Our analysis shows that cell centered fields are not really needed in upwind differentiation, even for Godunov-type schemes. In fact, the MHD system structure relies on two different kinds of magnetic field variables, depending on differentiation coordinates. The first set, given by the $[b_x(x,), b_y(, y)]$ variables, which are continuous in the indicated coordinates, satisfy the divergence-free condition and does not have a characteristic representation. The second one, given by $[B_x(, y), B_y(x,)]$, enters the characteristic space and can then have (transverse) discontinuities. The former quantities are advanced in time as staggered field data, while the latter can be reconstructed by interpolation either at a cell boundary or at a cell corner point.

As a last point, we comment here on the way the flux for the induction equations is derived. In the DW and BS schemes, the Ω fluxes (or electric fields components) are constructed by a simple arithmetic averages in space and for each 1-D upwind flux. This approach, which seems reasonable for second order accuracy, is not consistent since it does not reduce to the original 1-D fluxes when the discontinuity front propagates along one of the coordinate axes. This drawback led BS to introduce a rather empirical *switch* to select the dominant direction of front propagation. On the other hand, RY derives a formally correct flux, of the same form of our Eq. (26), by splitting the flux $\Omega = v_x B_y - v_y B_x$ into two independent components ($v_x B_y$ and $v_y B_x$), and 1-D independent upwindings along the x and y direction, respectively, have then been applied. However, this computational trick has no physical support, since the two characteristics spaces, spanned by the $\mathbf{A}_x$ and $\mathbf{A}_y$, in the original MHD equations are both based on the complete Ω flux.

4. Implementetion of a third order LF-CENO scheme

We consider the 2-D MHD system in cartesian (x, y) coordinates, in the conservation form given by Eqs. (17), to integrate the density, momenta and energy variables, and by Eq. (21) to integrate the vector potential. The updated, line-averaged, magnetic fields $(\overline{B}_x, \overline{B}_y)$ are defined, at each time step, by the geometrical relations Eqs. (14).

We specify the general procedure outlined in the previous Sect. 3 by choosing high order reconstruction algorithms based on convex-ENO (CENO) method, a local Lax-Friedrichs (LLF) flux splitting for upwinding and a time integration step using a third order TVD Runge-Kutta scheme.

All the indicated numerical ingredients are well

documented and tested in problems described by the Euler system of gas-dynamics (Shu & Osher 1988, for time integration, Shu 1997, for general ENO reconstruction and Liu & Osher 1998, for CENO method). It is then sufficient to detail here the specific procedures allowing to extend CENO schemes to the MHD system and having relevance to the divergence-free properties of the magnetic fields.

1. Among high order reconstruction algorithms, the recently proposed CENO method has the main computational advantage to avoid the time consuming characteristic decomposition of state variables, which is usually adopted in upwind schemes.

   To achieve this property, one consider first a TVD (monotone) second order accurate interpolant for the scalar variable $w(x)$ with data $\{w_j\}$, where w denotes any component of the state vector $\mathbf{w}$. In the $x_{j-1/2} \leq x \leq x_{j+1/2}$ range, three-point linear polynomials have the form

   $$L_j^{(k)}(x) = w_j + \frac{1}{h_x}[\Delta w]_{j+k}(x - x_j), \quad k = 0, 1$$

   where $[\Delta w]_i = w_{i+1} - w_i$. In classical TVD schemes a unique interpolant $\tilde{L}_j(x) = w_j + \frac{1}{h_x}[\mathcal{D}^{(1)}w]_j(x - x_j)$ with slope $[\mathcal{D}^{(1)}w]_j$ is chosen using min-mod (mm) limiters to assure nonoscillatory properties

   $$[\mathcal{D}^{(1)}w]_j = mm([\Delta w]_{j-1}, [\Delta w]_j).$$

   The $mm(a, b)$ function is defined, as usual, by

   $$mm(a, b) = sign(a)min[|a|, |b|], \quad ab > 0$$

   and $mm(a, b) = 0$ otherwise.

   Using the selected $\tilde{L}_j(w)$ polynomial, the interpolated values at the cell boundaries are then given by $[w^{(L)}]_{j+1/2} = \tilde{L}_j(x_{j+1/2})$, $[w^{(R)}]_{j+1/2} = \tilde{L}_{j+1}(x_{j+1/2})$.

   At any point of discontinuity as well at any smooth extrema of $w(x)$ where the first differences change sign, the TVD polynomial reduces to the constant state $\tilde{L}_j(x) = w_j$. Clipping to first order accuracy at a function jump is unavoidable in any polynomial based reconstruction, while higher ($r \geq 2$) accuracy in smooth ranges can always be achieved by enforced TVD or ENO procedures. This improvement, however, usually requires a preliminary decomposition of the $\Delta\mathbf{w}$ differences into characteristic modes, locally at each grid point. In the CENO method a higher order interpolation is maintained only at smooth regions while first order polynomials are used at the function jumps, neither cases requiring a characteristic decomposition.

   For third order reconstruction, in particular, one has at disposal three quadratic interpolants in the $x_{j-1/2} \leq x \leq x_{j+1/2}$ range

   $$Q_j^{(k)}(x) = w_i + \frac{1}{2}([\Delta w]_i + [\Delta w]_{i-1})\frac{(x - x_i)}{h_x}$$
   $$+\frac{1}{2}[\Delta^{(2)}w]_i\frac{(x - x_i)^2}{h_x^2},$$

   where $[\Delta^{(2)}]_i = [\Delta_i - \Delta_{i-1}]$ and centering refers to the index $i = j + k$ for $k = -1, 0, 1$. The CENO selection procedure allows to construct the unique nonoscillatory interpolant

   $$\tilde{Q}_j(x) = w_j + \frac{1}{2}[\mathcal{D}^{(1)}w]_j\frac{(x - x_j)}{h_x}$$
   $$+\frac{1}{2}[\mathcal{D}^{(2)}w]_j\frac{(x - x_j)^2}{h_x^2},$$

   which is *closest* to the TVD lower order interpolant $\tilde{L}_j(w)$. This is obtained by computing the three differences

   $$d_j^{(k)} = Q_j^{(k)} - \tilde{L}_j, \quad k = -1, 0, 1$$

   at the $x = x_{j-1/2}$ or $x = x_{j+1/2}$ boundary point. In a smooth range all these distance indicators have the same sign and one can select then

   $$\tilde{Q}_j = Q_j^{(k_0)}, \quad |d^{(k_0)}| = min_k|d^{(k)}|.$$

   Only at a discontinuity point at least one indicator changes sign and in this case one takes $\tilde{Q}_j = \tilde{L}_j = w_j$ since $\mathcal{D}^{(1)} = \mathcal{D}^{(2)} = 0$, clipping to a first order interpolation.

2. We apply then this reconstruction procedure, first to each $u_{j,k}$ scalar component of the $\mathbf{u}$ state vector, to recover the point values

   $$[u^{(L)}]_{j+1/2,k} = \tilde{Q}_j[u](x_{j+1/2}, y_k),$$

$$[u^{(R)}]_{j+1/2} = \tilde{Q}_{j+1}[u](x_{j+1/2}, y_k),$$

needed to compute the $\mathbf{f}(\mathbf{w}_x, B_x)$ flux , and in a similar way to recover the $u_{j,k+1/2}$ values needed to compute the $\mathbf{g}(\mathbf{w}_y, B_y)$ flux.

3. The definition of (B_x, B_y) point values introduced in Sect. 3 requires the specification of the nonoscillatory $\mathcal{D}^{(2)}$ second derivative. In the CENO framework one simply takes

$$\mathcal{D}_x^{(2)} = mm[\Delta_{j-1}^{(2)}, \Delta_j^{(2)}, \Delta_{j+1}^{(2)}],$$

$$\mathcal{D}_y^{(2)} = mm[\Delta_{k-1}^{(2)}, \Delta_k^{(2)}, \Delta_{k+1}^{(2)}].$$

We notice that this procedure returns the smoothest among the indicated three second numerical derivatives if the stencil of the involved first differences $[\Delta_{j-2}, ..., \Delta_{j+1}]$ is monotone, while $\mathcal{D}^{(2)} = 0$ if the first derivative has a jump or a smooth extremum.

For given $[\hat{B}_x]_{j+1/2,k}$, the reconstruction of the related divergence-free $[B_x]_{j+1/2,k}$ point values is given by the implicit definition in Eqs. (16)

$$[B_x - \gamma_1 \mathcal{D}_x^{(2)} B_x]_{j+1/2,k} = [\hat{B}_x]_{j+1/2,k},\ \gamma_1 = 1/24,$$

which we solve by using an explicit iteration procedure. By setting $B_x^{(0)} = \hat{B}_x$, at each $(x_{j+1/2}, y_k)$ point, the sequence

$$B_x^{(n)} = \hat{B}_x + \gamma_1 \mathcal{D}_x^{(2)}[B_x^{(n-1)}], \quad n = 1, 2, .. \quad (27)$$

is clearly rapidly convergent since $\mathcal{D}_x^{(2)}$ is at most an $O(h_x)$ quantity. In a similar way, we compute $[B_y]_{j,k+1/2}$ by iterating

$$B_y^{(n)} = \hat{B}_y + \gamma_1 \mathcal{D}_y^{(2)}[B_y^{(n-1)}], \quad B_y^{(0)} = \hat{B}_y. \quad (28)$$

In practical computations, for all the test problems presented in the next section, we found that $n = 5$ is sufficient to assure $\nabla \cdot \mathbf{B} = 0$ to within machine accuracy both in the maximum and in the L_1 norm.

The computed $[B_x]_{j+1/2,k}$ point values computed in Eq. (27) enter now the $\mathbf{f}(\mathbf{w}_x, B_x)$ flux as they stand, while the $[B_y]_{j+1/2,k}$ component of the $\mathbf{w}_x$ state vector needs a further interpolation. Using then $[B_y]_{j,k+1/2}$ derived by Eq. (28), the cell centered $[B_y]_{j,k}$ field is first reconstructed by taking

$$[B_y]_{j,k} = \frac{1}{2}([\tilde{B}_y]_{j,k-1/2} + [\tilde{B}_y]_{j,k+1/2}),$$

$$[\tilde{B}_y]_{j,k+1/2} = [B_y]_{j,k+1/2} - \frac{1}{8}[\mathcal{D}_y^{(2)} B_y]_{j,k+1/2},$$

to be finally interpolated at the $(x_{j+1/2}, y_k)$ cell boundary point like the other $u_{j,k}$ components of the $\mathbf{w}_x$ state vector. It is worth noticing that the cell centered $[B_y]_{j,k}$ values have not divergence-free properties since the $\mathbf{f}(\mathbf{w}_x, B_x)$ differentiation involves only the x coordinate.

By symmetric arguments, the $[B_y]_{j,k+1/2}$ field enters the $\mathbf{g}(\mathbf{w}_y, B_y)$ flux as it stands, while $[B_x]_{j+1/2,k}$ has now to be interpolated using the cell centered values

$$[B_x]_{j,k} = \frac{1}{2}([\tilde{B}_x]_{j-1/2,k} + [\tilde{B}_y]_{j+1/2,k}),$$

$$[\tilde{B}_x]_{j+1/2,k} = [B_x]_{j+1/2,k} - \frac{1}{8}[\mathcal{D}_x^{(2)} B_x]_{j+1/2,k}.$$

4. The interpolated $[\mathbf{w}_x]_{j+1/2,k}$ or $[\mathbf{w}_y]_{j,k+1/2}$ are represented as two-point left-right values along the relevant x or y coordinate, and an approximate Riemann solver has then to be specified to compute upwind fluxes. We have chosen the simple LLF flux composition, defined by

$$\mathbf{f}(\mathbf{w}_x, B_x) = \frac{1}{2}[\mathbf{f}(\mathbf{w}_x^{L,}, B_x) + \mathbf{f}(\mathbf{w}_x^{R,}, B_x)]$$

$$-\frac{1}{2}\alpha_x(\tilde{\mathbf{w}}_x)(\mathbf{u}^{R,} - \mathbf{u}^{L,}), \quad (29)$$

and

$$\mathbf{g}(\mathbf{w}_y, B_y) = \frac{1}{2}[\mathbf{g}(\mathbf{w}_y^{,L}, B_y) + \mathbf{g}(\mathbf{w}_y^{,R}, B_y)]$$

$$-\frac{1}{2}\alpha_y(\tilde{\mathbf{w}}_y)(\mathbf{u}^{,R} - \mathbf{u}^{,L}). \quad (30)$$

The scalar variable $\alpha_x(\tilde{\mathbf{w}}_x)$ is given at each $(x_{j+1/2}, y_k)$ point by the largest of the $\mathbf{A}_x$ matrix eigenvalues $\lambda_s(\tilde{\mathbf{w}}_x)$, and $\tilde{\mathbf{w}}_x$ is the arithmetic average of the $\mathbf{w}_x$ left-right states. In practice $\alpha_x = |v_x| + c_{f_x}$, where c_{f_x} is the fast wave speed along the x direction. Correspondingly, $\alpha_y(\tilde{\mathbf{w}}_y) = |v_y| + c_{f_y}$ gives the largest eigenvalue of the $\mathbf{A}_y$ matrix based on the arithmetic average of the left-right states of $\mathbf{w}_y$ at the $(x_j, y_{k+1/2})$ point.

5. Differences of flux values given in Eqs. (29), (30) provide only second order accurate derivatives, even if the reconstructed flux arguments share a higher accuracy order. To keep third order

in derivative approximations, we construct the primitives

$$\hat{\mathbf{f}}_{j+1/2,k} = [\mathbf{f} - \gamma_1 \mathcal{D}_x^{(2)} \mathbf{f}]_{j+1/2,k},$$

$$\hat{\mathbf{g}}_{j,k+1/2} = [\mathbf{g} - \gamma_1 \mathcal{D}_y^{(2)} \mathbf{g}]_{j,k+1/2}$$

thus completing the integration scheme of Eqs. (17) for the six-component state vector $\mathbf{u}_{j,k}$.

6. The $\Omega(\mathbf{w})$ flux variable needs a proper upwinding procedure, as shown in Eq. (26). In a LLF scheme one has

$$\Omega(\mathbf{w}_P) =$$

$$\frac{1}{4}[\Omega(\mathbf{w}^{(R,R)}) + \Omega(\mathbf{w}^{(R,L)}) + \Omega(\mathbf{w}^{(L,R)}) + \Omega(\mathbf{w}^{(L,L)})]_P$$

$$-\frac{1}{2}[\alpha_x(\tilde{\tilde{\mathbf{w}}})\delta_x B_y - \alpha_y(\tilde{\tilde{\mathbf{w}}})\delta_y B_x]_P, \qquad (31)$$

where all the arguments (v_x, v_y, B_x, B_y) are first interpolated at a common $P = (x_{j+1/2}, y_{k+1/2})$ point.

7. Finally, for time integration, a three-step Runge-Kutta algorithm provides the overall third order accuracy of the LF-CENO scheme.

5. Numerical results

The proposed numerical problems are mainly concerned with the divergence-free property, which on numerical side entails two main aspects:

1. the existence of a vector potential $A(x_{j+1/2}, y_{k+1/2}, t)$ as a continuous function at all times, assuring regular field lines topology (only corners are allowed),

2. a vanishing $D_B \equiv [\nabla \cdot \mathbf{B}]_{j,k}$ where field derivatives are computed using the same field components and the same difference algorithms as in dynamical flux calculations.

Since this form of validation has no counterpart in other proposed numerical works, comparisons with published data will cover necessarily rather qualitative aspects. Beside the divergence-free condition, the numerical results give also indications on the resolution properties, as well as on the stability and reliability of the MHD code described in the Sect. 4.

Finally, we remark that in our code the $A(x, y)$ vector potential refers only to the nonuniform (B_x, B_y) fields, since constant initial components are trivially preserved in time. Therefore, for problems having constant components (B_{0x}, B_{0y}), the evolved $A(t)$ field is now defined by

$$B_x = B_{0x} + \partial_y A, \quad B_y = B_{0y} - \partial_x A,$$

replacing the original Eqs. (10) of Sect. 2.

5.1. Shock-tube tests

We first consider 1-D Riemann problems (using a full 2-D grid) to check for resolution properties of the proposed scheme. To that purpose, it is necessary to take into account that high order schemes are not well suited for shock-tube problems where lower order characteristic-based schemes are optimal, instead.

We consider three problems documented by Ryu and Jones (1995) in their Fig 1a, Fig 2a and Fig 5a, which we here label RJ1, RJ2 and RJ3, correspondingly. In all the indicated cases a uniform grid with $N_x = 400$ grid points, a grid size $L_x = 1$, an adiabatic index $\gamma = 5/3$ and a CFL number $c = 0.8$, are used. In all numerical tests presented here, the parameters γ and c will always retain the same values.

In RJ1, the initial conditions for the state vector $\mathbf{w}(x) = [\rho, v_x, v_y, v_z, B_y, B_z, p]^T$ are defined by

$$\mathbf{w}^L = [1,\ 10,\ 0,\ 0,\ 5B_0,\ 0,\ 20]^T,$$

$$\mathbf{w}^R = [1,\ -10,\ 0,\ 0,\ 5B_0,\ 0,\ 1]^T,$$

and by a constant $B_{0x} = 5B_0$. Here left states refer to $x < 0.5$ and right states to $x > 0.5$. The unit magnetic field is $B_0 = 1/\sqrt{4\pi}$. In Fig. 1 the evolved variables (ρ, p, B_y, v_x) are shown at time $t = 0.08$, as in the referenced RJ paper.

In the RJ2 test initial conditions are defined by

$$\mathbf{w}^L = [1.08,\ 1.2,\ 0.01,\ 0.5,\ 3.6B_0,\ 2B_0,\ 0.95]^T,$$

$$\mathbf{w}^R = [1,\ 0,\ 0,\ 0,\ 4B_0,\ 2B_0,\ 1]^T,$$

and the constant magnetic field is now $B_{0x} = 2B_0$. The evolved variables $(\rho, p, B_y, v_y, B_z, v_z)$ at time $t = 0.2$ are shown in Fig. 2.

Finally, the RJ3 problem, with initial data

$$\mathbf{w}^L = [1, 0, 0, 0, 1, 0, 1]^T,$$

$$\mathbf{w}^R = [0.125, 0, 0, 0, -1, 0, 0.1]^T,$$

and $B_{0x} = 0.75$, is illustrated in the Fig. 3, for $t = 0.1$. This is already considered a classical test, related to the presence of a compound wave (Brio & Wu 1988).

As can be seen, the plotted results reproduce well all the main expected features and compare with the corresponding results obtained with higher grid resolutions and more elaborate Riemann solvers (Ryu & Jones 1995, Jiang & Wu 1999). Postshock oscillations, which are always produced in any shock-capturing scheme (Arora & Roe 1996), appear here with vanishing amplitudes behind the fast moving shocks but have significant sizes near the slow shocks and near the expansion wave on the right hand side of Fig. 3. At present, to our knowledge, no general cure has been envisaged to suppress entirely this unphysical wave noise, which can then only be reduced by adding numerical viscosity. In this sense, the observed oscillations allow to estimate the implicit numerical viscosity of our CENO-LF scheme to be somehow intermediate between the lower order TVD code of Ryu & Jones (1995) and the Weno-LLF MHD code of Jiang & Wu (1999). Other limiters have also been tested (van Leer, *superbee*, and so on), with no significant improvements. In any case, we want to stress again the point that high order schemes not based on characteristics decomposition, like our code, are not particularly designed to handle Riemann problems, where a lower order scheme may be a better choice.

To test the code for 2-D cases, we have run the previous Riemann problems RJ1 and RJ2 with structures propagating along the main diagonal of a computational box with sizes $L_x = \cos\alpha$, $L_y = \sin\alpha$, where $\alpha = \pi/4$. In this way the diagonal has a unit size $L = 1$ and $h = 1/N_x$ is the size of the cell diagonals. Initial conditions are then assigned to the state vector $\mathbf{w}(\xi) = [\rho, v_\xi, v_\eta, v_z, B_\eta, B_z, p]^T$ along the coordinate $\xi = x\cos\alpha + y\sin\alpha$, with now $B_\xi = B_{0\xi}$ being constant. Boundary conditions are specified by imposing the continuity of all variables along the traverse direction $\eta = y\cos\alpha - x\sin\alpha$, extended to the $x < 0$, $x > L_x$ and to the $y < 0$, $y > L_y$ sides. We used $N_x = N_y = 256$ grid points and we found that this grid spacing is hardly sufficient to recover the main flow structures.

The evolved variables $\mathbf{w}(\xi)$ are shown in Fig. 4 for the rotated 1-D Riemann problem of Fig. 1, and in Fig. 5 for the rotated 1-D Riemann problem of Fig. 2, at corresponding times. The plotted results compare to the ones presented by Ryu et al. (1998) for the same Riemann problems. The fact that the small oscillations observed in the corresponding 1-D cases are now less apparent, is due to the higher numerical dissipation produced by the lower resolution.

In a 2-D shock-tube problem, the divergence-free condition can be simply expressed by a constant B_ξ field, *i.e.* by the $dB_\xi/d\xi = 0$ relation along both the ξ and η coordinates. However, if B_ξ is constructed using the cell centered $[B_x, B_y]_{j,k}$ fields, this conservation law is poorly verified, as can be seen in Fig. 6a, where the numerical derivative $\Delta_\xi B_\xi/h$ for the RJ2 test is plotted. On the other hand, using the vector potential, point values of the B_ξ field are properly defined by

$$B_\xi = B_{0\xi} + \frac{\partial A}{\partial \eta}$$

and the divergence-free condition results if A (as well as the other dynamical variables) do not depend on the η coordinate. This is documented by the 2-D structure shown in Fig. 6b. The corresponding numerical derivative

$$\frac{1}{h}\Delta_\xi B_\xi = \frac{\Delta_\xi \Delta_\eta A}{h^2}$$

has now a maximum size of $\simeq 10^{-5}$.

5.2. Slow wave steepening and shock formation

Nonlinear wave steepening from continuous initial data is a main feature of compressible flows. In the MHD case this problem has also interesting astrophysical aspects for the study of intermediate shocks (shocks coupled to expansion waves), already encountered in the previous shock-tube test RJ3. On the computational side, wave steepening is significant for high order schemes, whose small numerical dissipation may model weakly resistive plasmas. Reference results are given by Wu (1987) for physical setting in resistive MHD and by Dai & Woodward (1998) and Jiang & Wu (1999) for numerical testing.

Here we consider initial data defined by a (smooth) slow wave front propagating along the transverse ξ axis, with a slope angle $\alpha = \pi/6$ with respect to the x axis. The initial conditions are defined by the characteristic differential equations (the prime here denoting a ξ derivative)

$$\rho' = -\frac{B_\eta B'_\eta}{(a^2 - c_s^2)},\; p' = a^2\rho',\; q'_\xi = \frac{c_s}{\rho}\rho',\; q'_\eta = \frac{c_f}{a\sqrt{\rho}}B'_\eta,$$

relating (ρ, p, q_ξ, q_η) to the B_η field along the ξ coordinate. The variables a, c_s, c_f denote the sound, slow and fast wave speeds, respectively. We choose as initial profile $B_\eta(\xi) = \sin(2\pi\xi)$ and a cartesian box

with $L_x = 1/\cos\alpha$ and $L_y = 1/\sin\alpha$, so that periodic boundary conditions can be applied along the x and y cartesian coordinates.

In Fig. 7 the ξ profiles of the variables (ρ, p, B_η, v_ξ) are shown at time $t = 1$, when a shock train is already formed. The corresponding 2-D plots of the pressure $p(x, y)$ and of the vector potential $A(x, y)$ are also shown in the Fig. 8, to check for accurate η independence of the flow variables. As for the previous shock-tube test of Fig. 6, a vanishing numerical $\nabla \cdot \mathbf{B}$ comes from the $\partial_\eta A \simeq 0$ condition. In Fig. 9a a surface plot of the variable D_B is also shown, giving a value $|D_B|_{max} \simeq 10^{-4}$ for the residual numerical monopoles, while the B_ξ component based on $(B_x, B_y)_{j,k}$ values shows a much higher derivative $O(10^{-1})$, as can be seen in the Fig. 9b.

5.3. The Orszag-Tang MHD vortex problem

A well known model problem to study the transition to MHD turbulence is provided by the so-called Orszag-Tang vortex, which has been extensively studied in its compressible version (for low Mach numbers) by many authors using spectral methods. For initial Mach numbers $M \geq 1$ this is also a valuable test for upwind codes, and it has been used for almost all the latest schemes (Zachary et al. 1994, Dai & Woodward 1998, Ryu et al. 1998, Jiang & Wu 1999). The referenced Orszag-Tang system is defined by the initial conditions

$$v_x = B_x/B_0 = -\sin 2\pi y, \quad v_y = \sin 2\pi x,$$

$$B_y = B_0 \sin 4\pi x, \quad p = (\beta/2)B_0^2, \quad \rho = \gamma p,$$

where $B_0 = 1/\sqrt{4\pi}$ and $\beta = 2\gamma$ for the usual $\gamma = 5/3$ value. The initial flow is the given by a velocity vortex superimposed to a magnetic vortex, with a common (singular) X-point, but with a different modal structure. This configuration is strongly unstable, giving rise to a wide spectrum of propagating MHD modes and shock waves (here the initial Mach number is $M = 1$), and to the transformation of the initial X-point to a current-sheet triggering the reconnection process.

For this test we have chosen a unit grid $L_x = L_y = 1$ with $N_x = N_y = 192$ collocation points. In Fig. 10 we present the pressure p and potential A isocontours at t=0.5, showing the good qualitative agreement with the other published works. In particular, 1-D profiles of the $p(x)$ variable at $y = 0.4277$ (upper plot) and at $y = 0.3125$ (lower plot) are shown in Fig. 11 for a more detailed comparison with the corresponding plots given, respectively, by Ryu et al. (1998) and Jiang & Wu (1999). The latter reference also contains some quantitative estimate of how significant magnetic monopoles may affect the computed solutions, thus producing numerical instabilities in a long time evolution.

The monopole distribution D_B (not plotted here) show only a few enhanced values $\simeq 10^{-5}$, thus assuring vanishing $\nabla \cdot \mathbf{B}$ condition. in the long time computations we found no evidence of negative pressure nor other unphysical behaviors. To check this point in more detail, we plot the magnetic field lines at $t = 3$ in Fig. 12, showing how the regularity of fieldlines is well preserved in time. This essential feature of the computed divergence-free magnetic field allows to reproduce typical magnetic phenomena, like the topology change induced by a vanishing resistivity (here modeled by a low numerical diffusivity). In fact, by comparing the latter A distribution with the former shown in Fig. 10, it is apparent how the initial magnetic islands around the X-point merge by reconnection.

5.4. Strong blast wave in free space

The following two numerical tests concern the formation and propagation of strong MHD discontinuities in a 2-D domain. These model problems are representative of many astrophysical phenomena where the magnetic energy has relevant dynamical effects. In numerical schemes having poor divergence-free properties, the (possible) onset of spurious solutions and of a negative gas pressure is clearly enhanced in these physical regimes, since the magnitude of numerical monopoles increases along with the background magnetic pressure. This problem has been discussed, in particular, by Balsara & Spicer (1999), where also some quantitative estimate of the numerical $\nabla \cdot \mathbf{B}$ produced by Godunov schemes has been documented.

The first test problem concerns the explosion of a circular dense cloud in a magnetized, initially static region. Here we take again a square domain with $N_x = N_y = 192$ grid points. Initial conditions are specified by filling a circular region located at the center and radius $r_0 = 0.125$ with a hot gas having $p = 100$. The background static fluid is characterized by $\rho = p = 1$ and $B_{0x} = 10$.

In Fig. 13 we show the density ρ, the magnetic potential A, the magnetic pressure $(B_x^2 + B_y^2)/2$ and the

solenoidal variable D_B distributions at time $t = 0.02$, which is already representative of the generated complex flow structure. In particular, the plotted results show the well preserved initial axial symmetries (around both the $y = 0.5$ and the $x = 0.5$ axis) as well as the regularity of magnetic fieldlines. As we can see, the resulting numerical D_B variable has an isolated peak with magnitude 10^{-3} and otherwise vanishing sizes $< 10^{-5}$.

5.5. The fast rotor problem

In the Balsara & Spicer (1999) work, a model problem to study the onset and propagation of strong torsional Alfvén waves, relevant for star formation, has been presented and analyzed. Following this reference, we have runned the same problem using a square unit computational box and $N_x = N_y = 240$ grid points. For propagating structures not intersecting the box boundaries, periodic conditions can be applied. Initial conditions are specified by a rapidly rotating cylinder (the rotor) with center at the $x = 0.5$, $y = 0.5$ point and radius $r = 0.1$. The rotor has (initial) density $\rho = 10$, angular velocity $\omega = 20$ and it is embedded in a static and uniform fluid with $\rho = p = 1$ and $B_{0x} = 2.5/\sqrt{\pi}$.

The flow pattern evolved at time $t = 0.18$ (just before the shocked flow reaches the boundaries) is shown in Fig. 14, representing as in Fig. 13 the space distribution of the density ρ, the magnetic potential A, the magnetic pressure $(B_x^2 + B_y^2)/2$ and the solenoidal variable D_B, that keeps everywhere below 4×10^{-4}. Even if a lower resolution than in the referenced paper is here adopted, and no smoothing has been applied to the initial density and rotation velocity discontinuities, the numerical results give convincing evidence on how a higher order scheme provides accurate and well resolved profiles even when strong discontinuities develop.

6. Conclusions

We have introduced a general method to adapt upwind schemes developed for Euler system to the corresponding MHD system in order to assure the divergence-free condition. The proposed approach can be applied to existing MHD codes as well as to any higher order extensions.

The use of a staggered collocation for the magnetic field components entering the $\nabla \cdot \mathbf{B}$ variable and of the related magnetic potential A are well known general premises to represent a numerical divergence-free magnetic field at the second order accuracy level. We have thus introduced proper algorithms to extend this representation to higher orders and to formulate upwind flux derivatives using only the divergence-free variables, in order to avoid the onset of numerical monopoles in the momentum and energy equations. Moreover, by taking into account consistency arguments, we have proposed a new formulation for the upwind flux for the induction equations.

As an application, we have constructed a simple and efficient third order LF-CENO based MHD code running in multidimensional systems. This code appear well suited for many astrophysical problems where, beside strong shocks, reconnection phenomena, complex wave patterns and turbulence develop, as confirmed by the several numerical tests here presented.

The authors would like to thank Marco Velli for many helpful discussions and for his support in completing this work.

REFERENCES

Arora, M., & Roe, P.L. 1996, J. Comp. Phys., 130, 25

Balsara, D.S. 1998a, ApJS, 116, 119

Balsara, D.S. 1998b, ApJS, 116, 133

Balsara, D.S. & Spicer, D.S. 1999, J. Comp. Phys., 149, 270

Barmin, A.A., Kulikovskiy, A.G., & Pogorelov, N.V. 1996, J. Comp. Phys., 126, 77

Brackbill J.U., & Barnes, D.C. 1980, J. Comp. Phys., 35, 426

Brio, M., & Wu, C.C. 1988, J. Comp. Phys., 75, 400

Cargo, P., & Gallice, G. 1997, J. Comp. Phys., 136, 446

Chen, G.-Q. & Lefloch, P.G. 1995, Comm. Pure Appl. Math, XLVIII, 691

Dai, W., & Woodward, P.R. 1998, ApJ, 494, 317

DeVore, C.R. 1991, J. Comp. Phys., 92, 142

Evans, C., & Hawley, J.F. 1988, ApJ, 332, 659

Harten, A. 1983, J. Comp. Phys., 49, 357

Harten, A., Engquist, B., Osher, S., & Chakravarthy, S. 1987, J. Comp. Phys., 71, 231

Harten, A., Lax, P.D., Levermore, C.D., & Morokoff, W.J. 1998, SIAM J. Numer. Anal., 35, 2117

Jiang, G.-S., & Wu, C.-C. 1999, J. Comp. Phys., 150, 561

Jin, S., &, Xin, Z. 1998, SIAM J. Numer. Anal., 35, 2385

Liu, X.-D., & Osher, S. 1998, J. Comp. Phys., 142, 304

Powell, K.G. 1994, ICASE Rep. No. 94-24

Roe, P.L., & Balsara, D.S. 1996, SIAM J. Numerical Anal., 56, 57

Ryu, D., & Jones, T.W. 1995, ApJ, 442, 228

Ryu, D., Jones, T.W., & Frank, A. 1995, ApJ, 452, 785

Ryu, D., Miniati, F., Jones, T.W., & Frank, A. 1998, ApJ, 504, 244

Shu, C.-W. 1997, ICASE Report No. 97-65, Langley, VA

Shu, C.-W., & Osher, S. 1988, J. Comp. Phys., 77, 439

Shu, C.-W., & Osher, S. 1989, J. Comp. Phys., 83, 32

Stone, J.M., & Norman, M.L. 1992, ApJS, 80, 791

Tadmor, E. 1988, ICASE Report No. 88-41

van Leer, B. 1979, J. Comp. Phys., 32, 101

van Leer, B. 1982, in Lecture Notes in Physics, 170, 507 (Berlin: Springer)

Wu, C.-C. 1987, Geophys. Res. Lett. 14, 668

Zachary, A.L., Malagoli, A., & Colella, P. 1994, SIAM J. Sci. Stat. Comput., 15, 263

This 2-column preprint was prepared with the AAS LaTeX macros v4.0.

Fig. 1.— The indicated variables at time $t = 0.08$ for the 1-D Riemann problem RJ1, using $N_x = 400$ grid points.

Fig. 2.— The indicated variables at time $t = 0.2$ for the 1-D Riemann problem RJ2, using $N_x = 400$ grid points.

Fig. 3.— The indicated variables at time $t = 0.1$ for the 1-D Riemann problem RJ3, using $N_x = 400$ grid points.

Fig. 4.— The same shock-tube problem as in Fig. 1, now along the main diagonal ξ of a 2-D square computational box with (256×256) grid points.

Fig. 5.— The same shock-tube problem as in Fig. 2, now along the main diagonal ξ of a 2-D square computational box with (256×256) grid points.

Fig. 6.— Left panel (a): the ξ derivative of the B_ξ field in the 2-D shock-tube problem of Fig. 5. Right panel (b): the corresponding isocontours of the magnetic potential A, which clearly show the η-invariance.

Fig. 7.— The indicated variables for the 2-D slow wave problem, along the ξ coordinate and at time $t = 1$. The slope angle is $\alpha = \pi/6$ and the computational box has (192×192) grid points.

Fig. 8.— The pressure (left) and magnetic potential (right) isocontours for the slow wave problem of Fig. 7 at the same time $t = 1$.

Fig. 9.— Left panel (a): A surface plot of $\nabla \cdot \mathbf{B}$ for the slow wave problem at time $t = 1$. Right panel (b): The numerical derivative of the B_ξ field, computed with cell centered (B_x, B_y) data.

Fig. 10.— The pressure (left) and magnetic potential A distribution (right) in the Orszag-Tang problem at time $t = 0.5$. The unit square computational box has (192×192) grid points.

Fig. 11.— The 1-D pressure distribution for the same problem as in Fig. 10 along a cut at $y = 0.4277$ (upper plot) and at $y = 0.3125$ (lower plot, where a proper normalized pressure is shown, to compare with the Jiang & Wu (1999) data).

Fig. 12.— The magnetic potential A distribution for the same problem as in Fig. 10 at a later time $t =$ 3. The reconnected central magnetic island is clearly shown.

Fig. 13.— The indicated variables at time $t = 0.02$ for the blast wave problem. A unit computational box is used with (192×192) grid points.

Fig. 14.— The indicated variables at time $t = 0.18$ in the rotor problem. A unit computational box is used with (240×240) grid points.

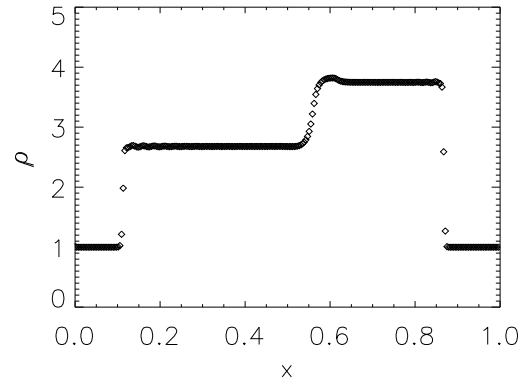
ρ
x
0
1
2
3
4
5
0.0
0.2
0.4
0.6
0.8
1.0

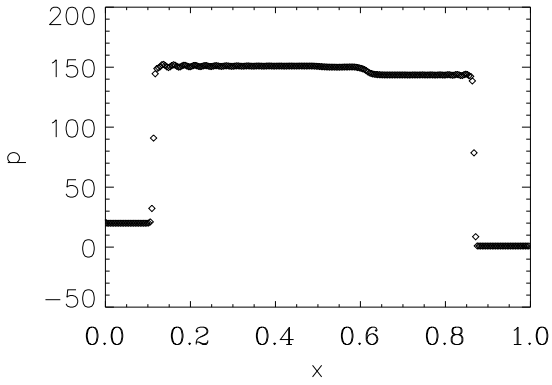
p
x
−50
0
50
100
150
200
0.0
0.2
0.4
0.6
0.8
1.0

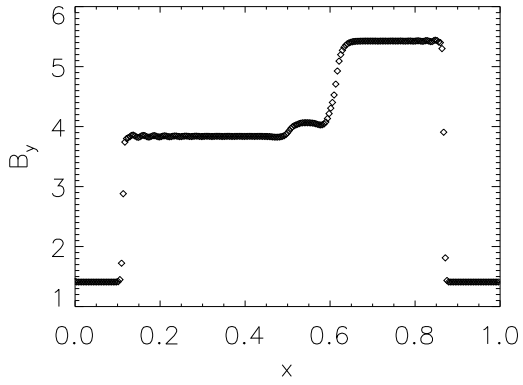
B_y
x
1
2
3
4
5
6
0.0
0.2
0.4
0.6
0.8
1.0

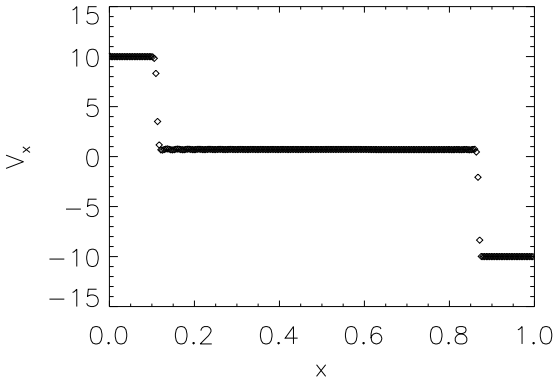
V_x
x
−15
−10
−5
0
5
10
15
0.0
0.2
0.4
0.6
0.8
1.0

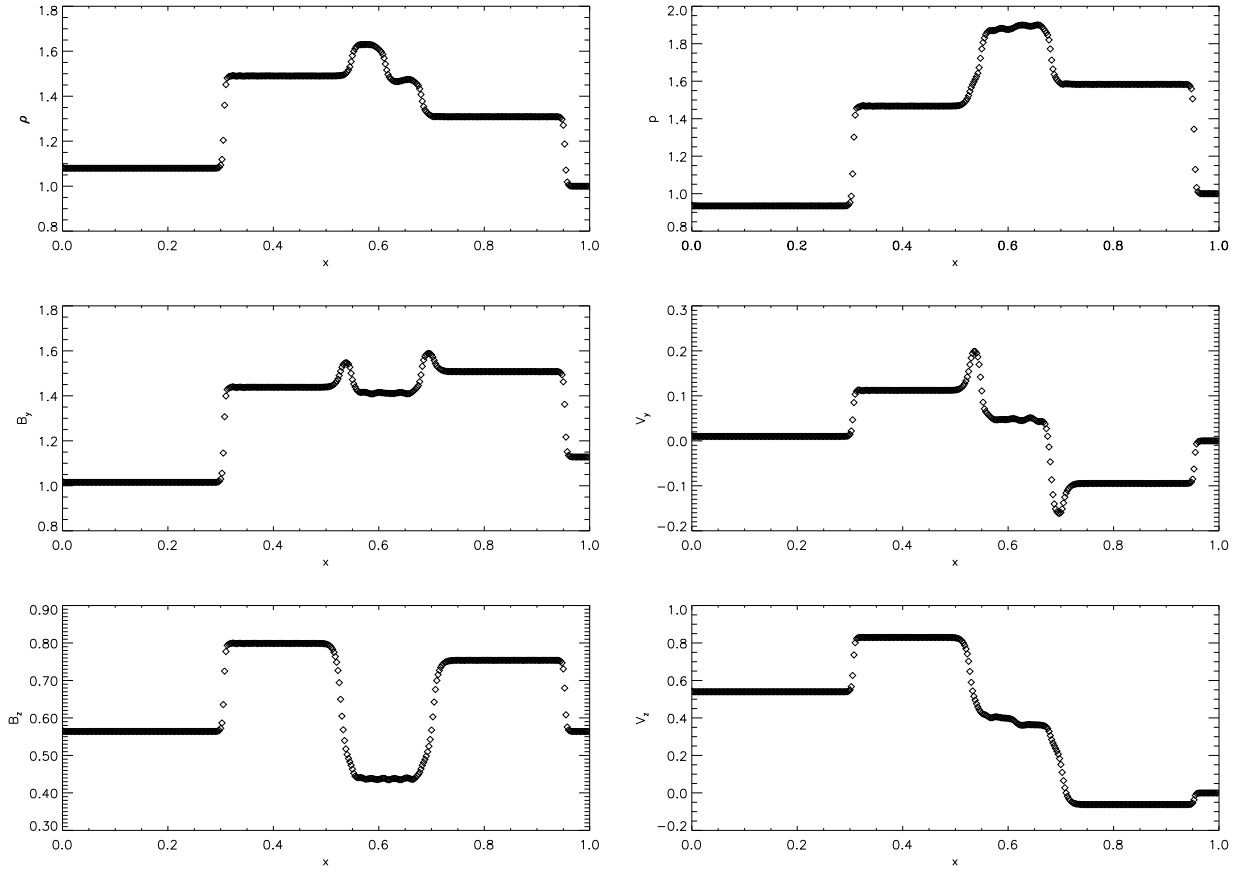
ρ
x
p
x
B_y
x
V_y
x
B_z
x
V_z
x

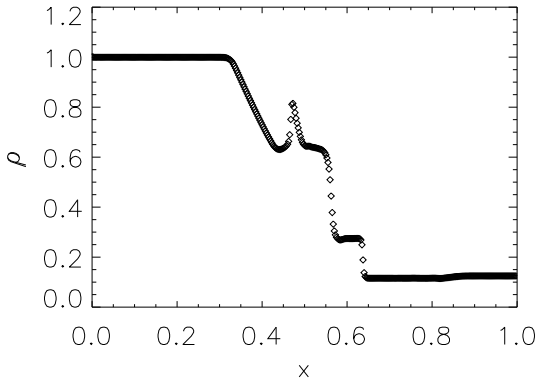
ρ
x

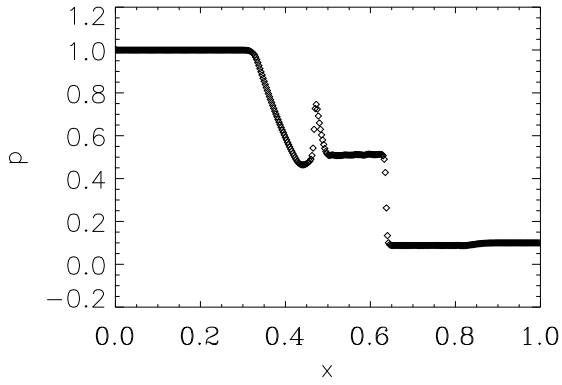
p
x

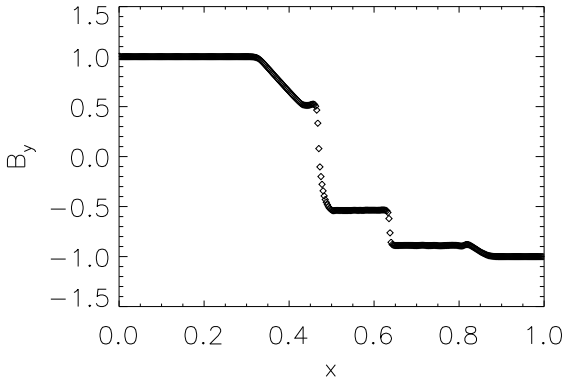
B_y
x

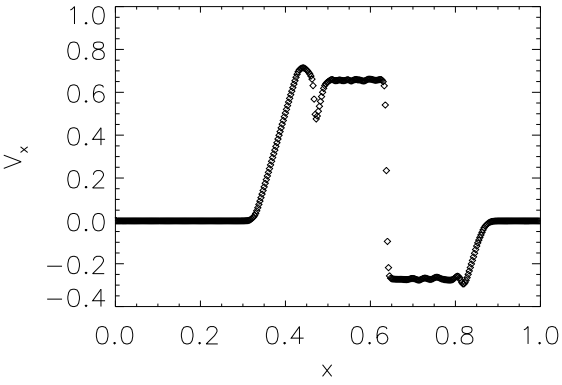
V_x
x

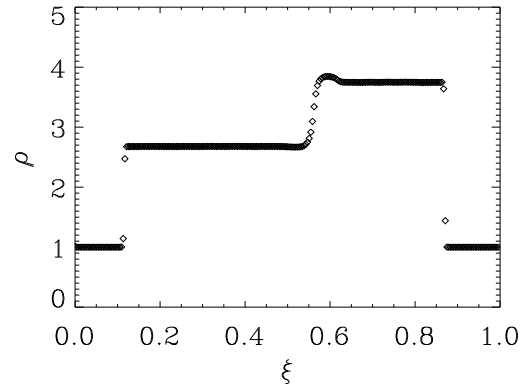
ρ
ξ

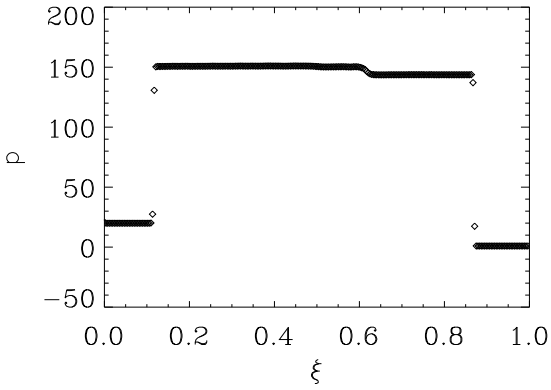
p
ξ

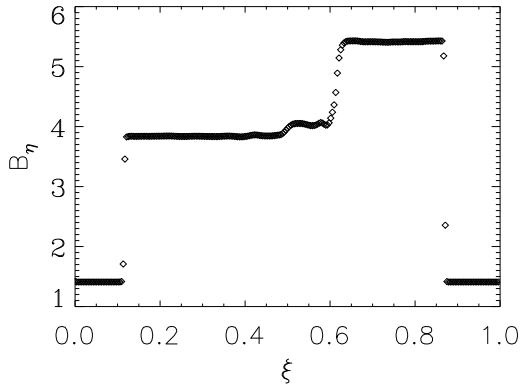
B_η
ξ

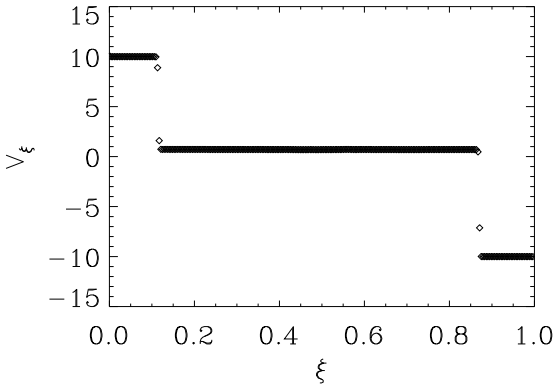
V_ξ
ξ

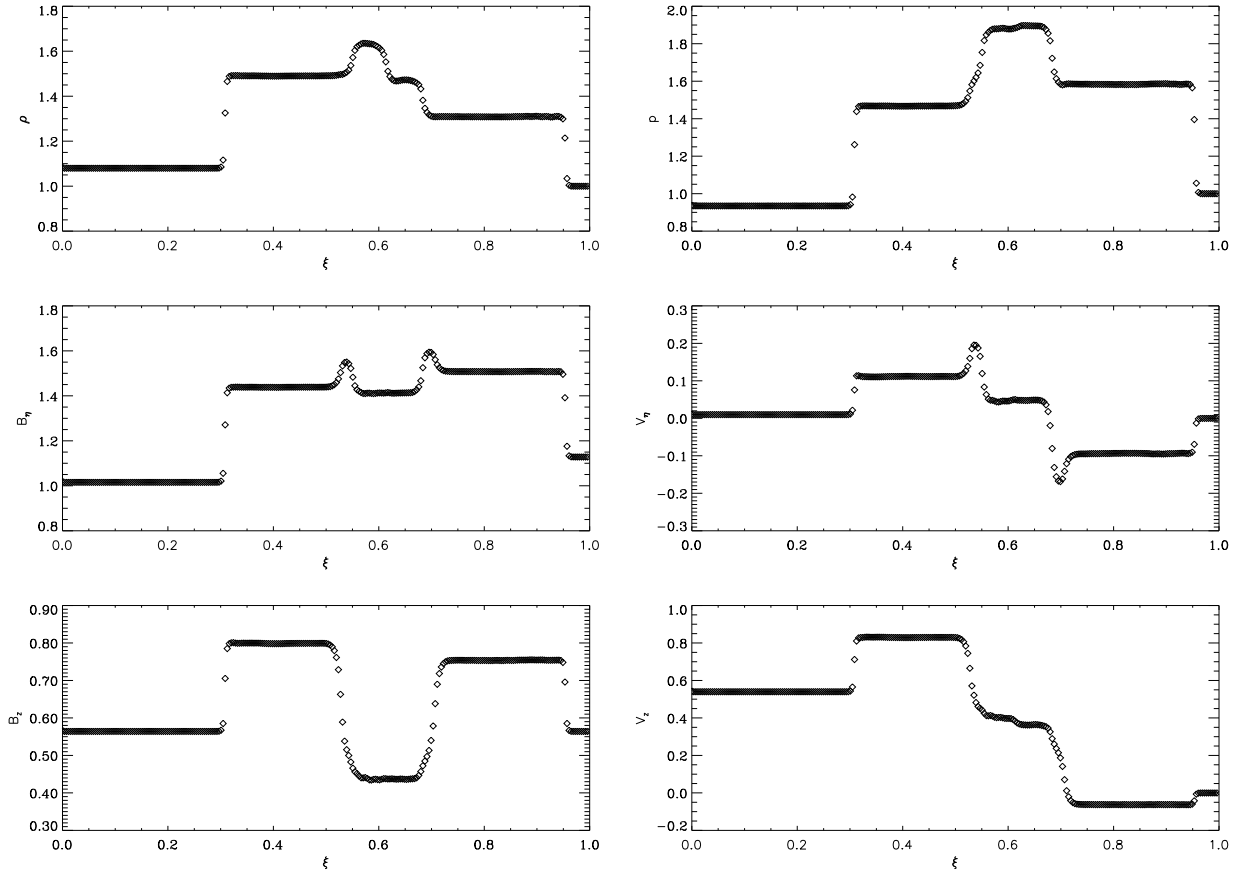
ρ
ξ
p
ξ
B_η
ξ
V_η
ξ
B_z
ξ
V_z
ξ

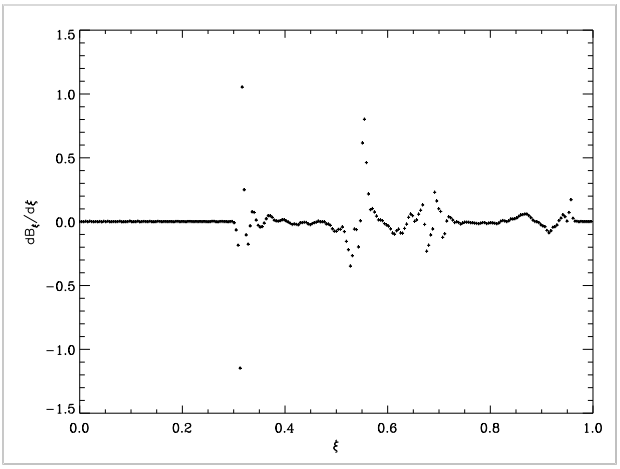
1.5
1.0
0.5
0.0
−0.5
−1.0
−1.5
dB_t/dξ
0.0
0.2
0.4
0.6
0.8
1.0
ξ

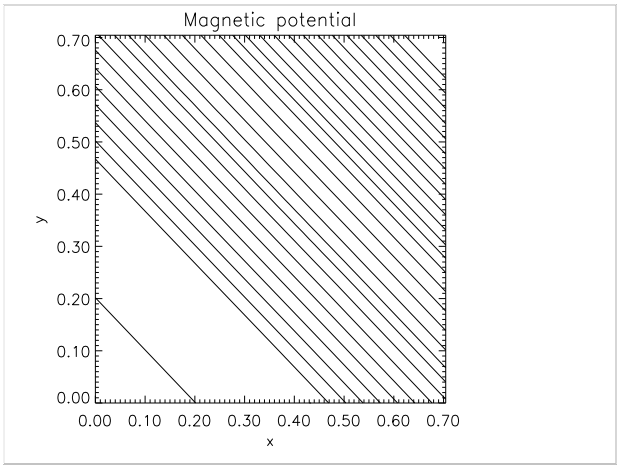
Magnetic potential
0.70
0.60
0.50
0.40
0.30
0.20
0.10
0.00
y
0.00 0.10 0.20 0.30 0.40 0.50 0.60 0.70
x

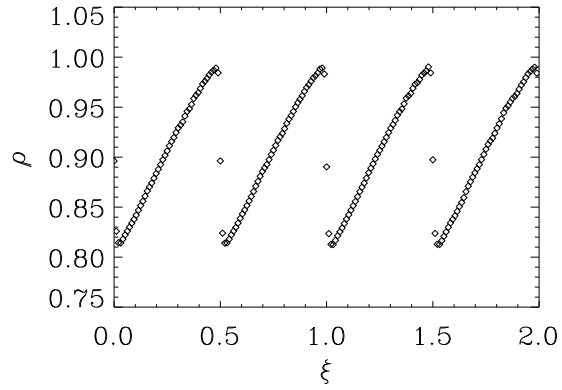
1.05
1.00
0.95
0.90
0.85
0.80
0.75
ρ
0.0
0.5
1.0
1.5
2.0
ξ

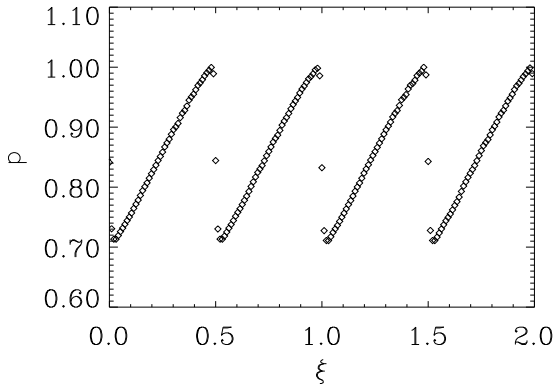
1.10
1.00
0.90
0.80
0.70
0.60
p
0.0
0.5
1.0
1.5
2.0
ξ

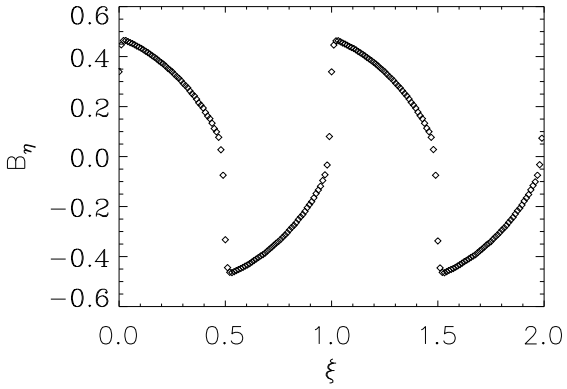
0.6
0.4
0.2
0.0
−0.2
−0.4
−0.6
B_η
0.0
0.5
1.0
1.5
2.0
ξ

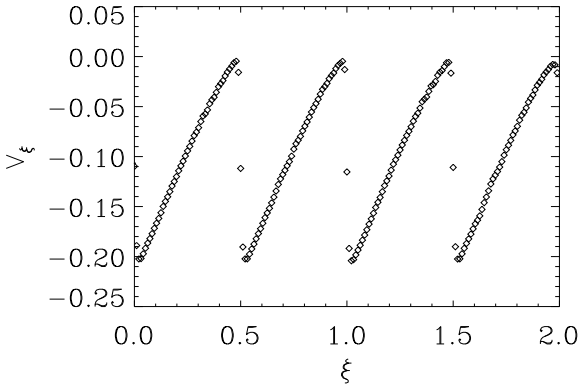
0.05
0.00
−0.05
−0.10
−0.15
−0.20
−0.25
V_ξ
0.0
0.5
1.0
1.5
2.0
ξ

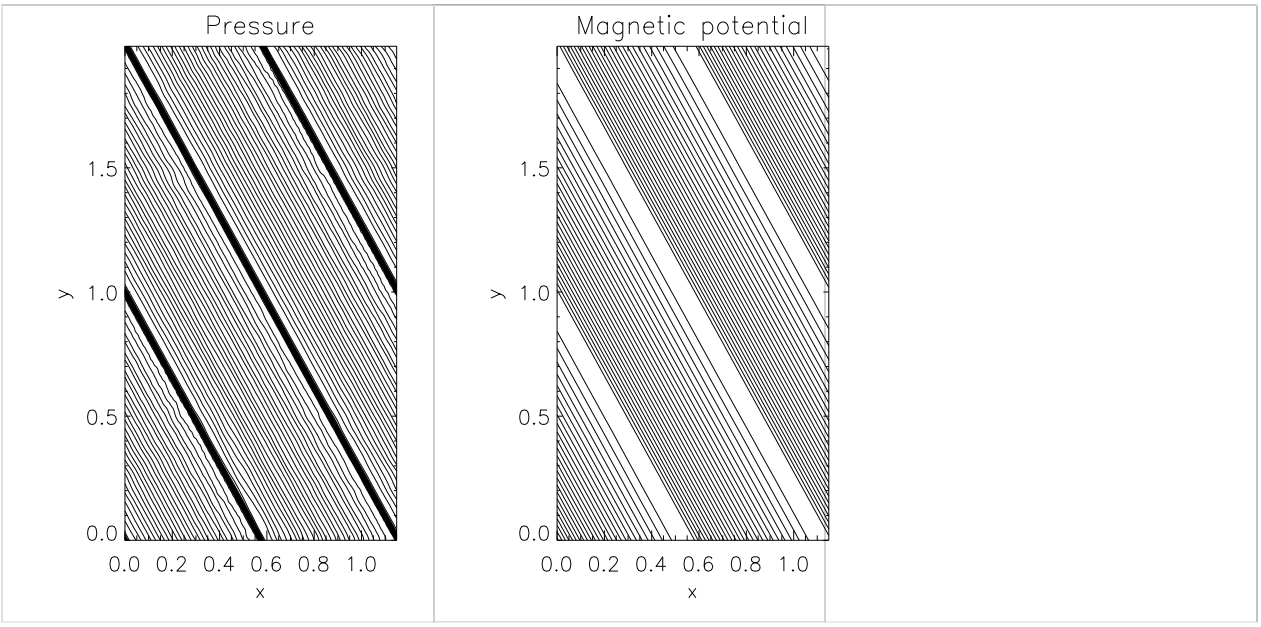
Pressure
Magnetic potential
y
x
0.0
0.5
1.0
1.5
0.0 0.2 0.4 0.6 0.8 1.0

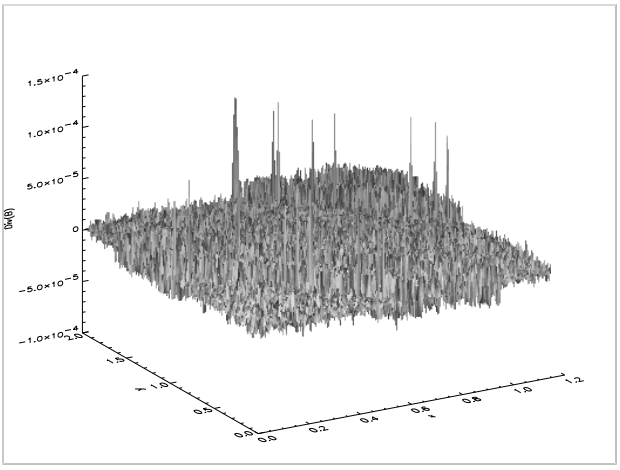
1.5×10⁻⁴
1.0×10⁻⁴
5.0×10⁻⁵
0
−5.0×10⁻⁵
−1.0×10⁻⁴
δw(θ)
0.0
0.2
0.4
0.6
0.8
1.0
1.2

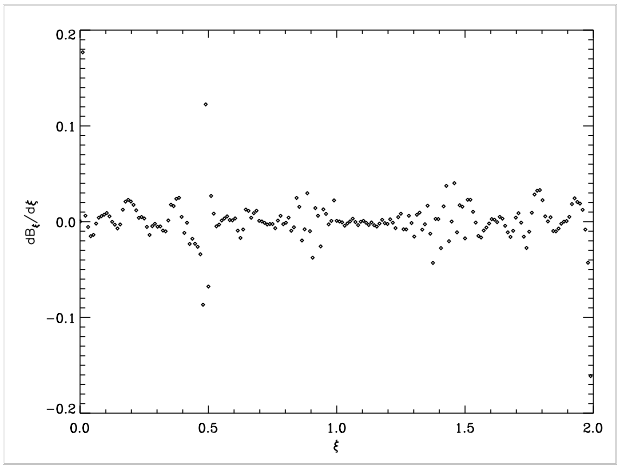
0.2
0.1
0.0
−0.1
−0.2
dB_r/dξ
0.0
0.5
1.0
1.5
2.0
ξ

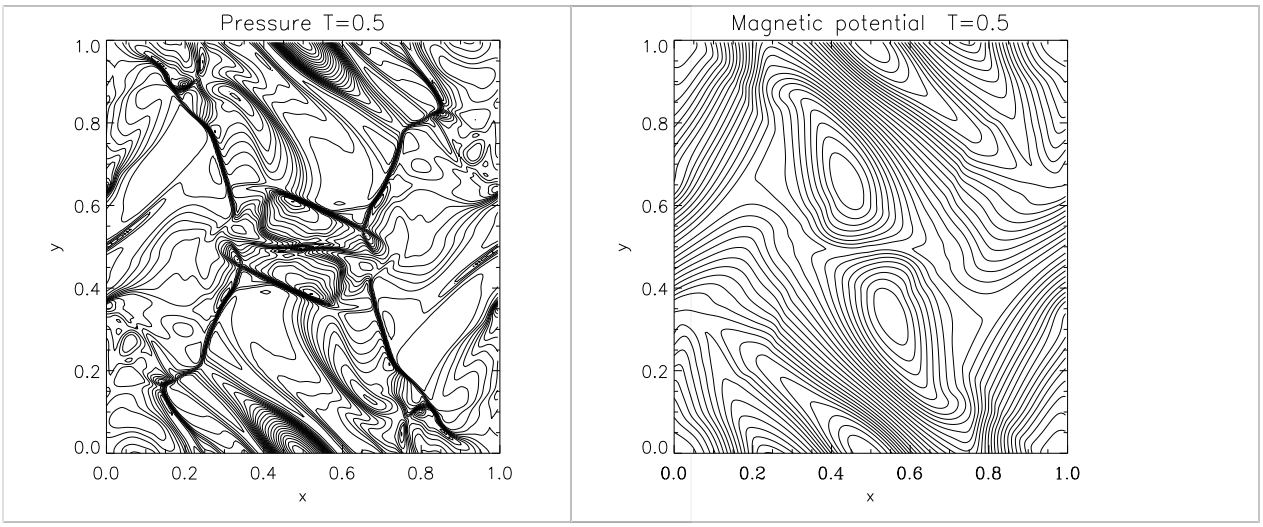
Pressure T=0.5
Magnetic potential T=0.5
x
y
0.0
0.2
0.4
0.6
0.8
1.0

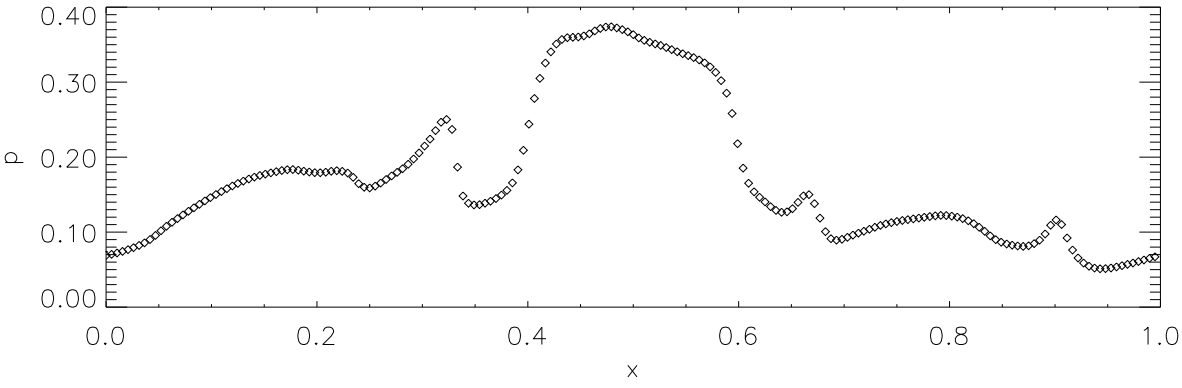
0.40
0.30
0.20
0.10
0.00
p
0.0
0.2
0.4
0.6
0.8
1.0
x

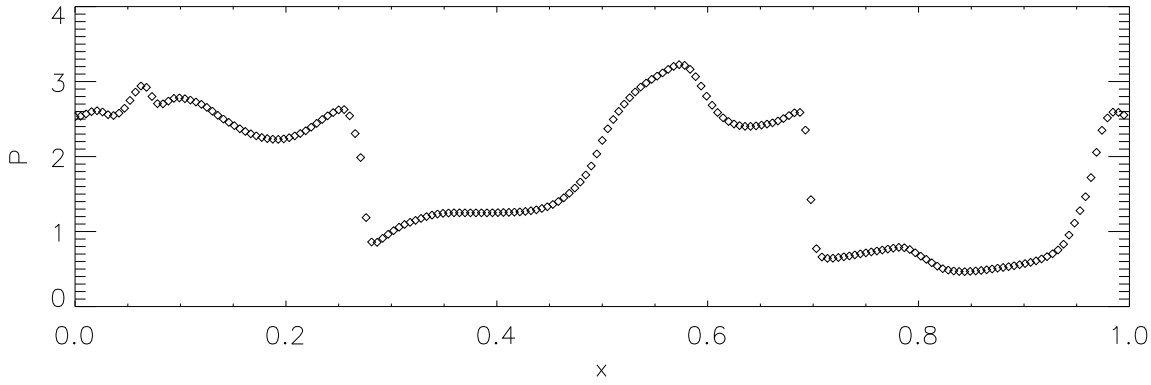
4
3
2
1
0
P
0.0
0.2
0.4
0.6
0.8
1.0
x

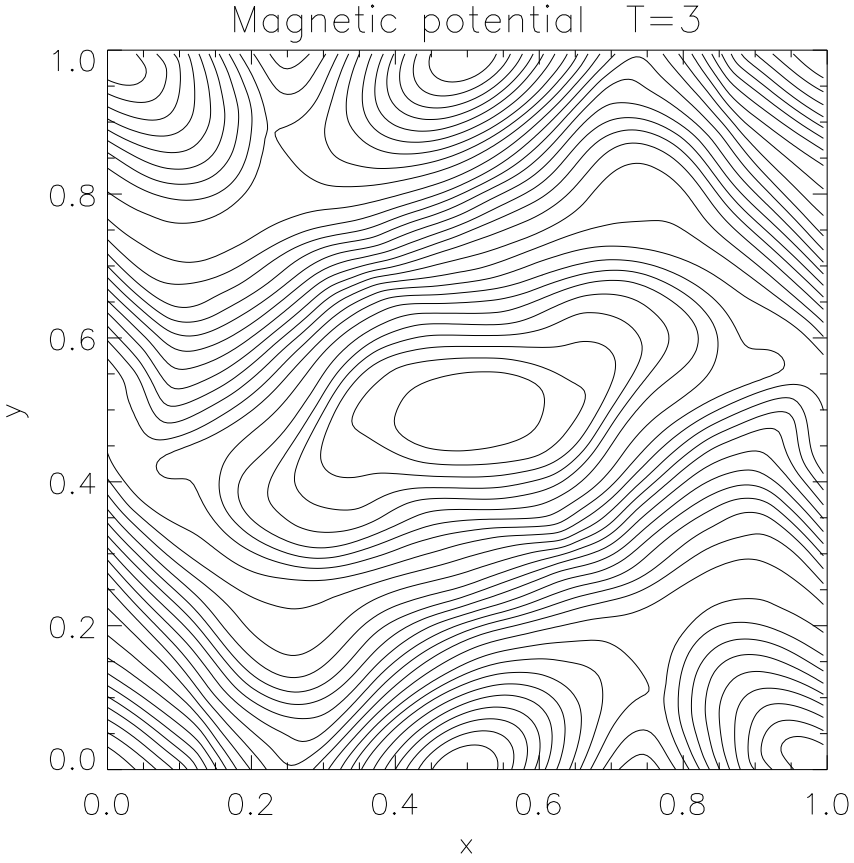
Magnetic potential T=3
1.0
0.8
0.6
0.4
0.2
0.0
y
0.0
0.2
0.4
0.6
0.8
1.0
x

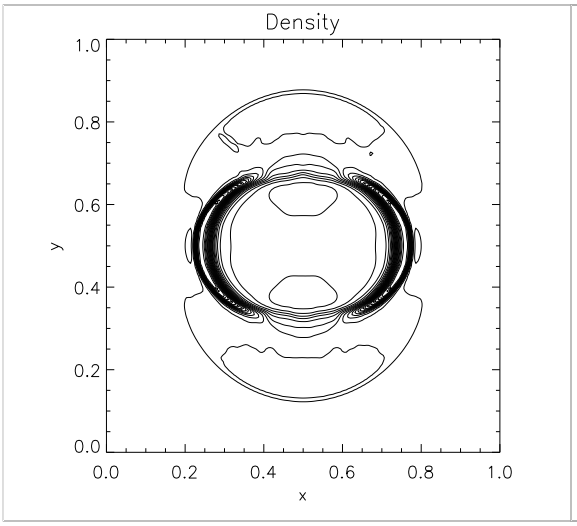
Density
1.0
0.8
0.6
0.4
0.2
0.0
y
0.0
0.2
0.4
0.6
0.8
1.0
x

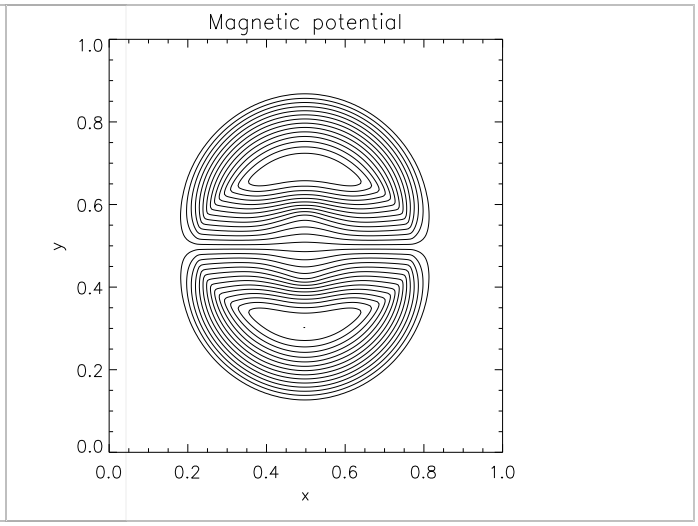
Magnetic potential
1.0
0.8
0.6
0.4
0.2
0.0
y
0.0
0.2
0.4
0.6
0.8
1.0
x

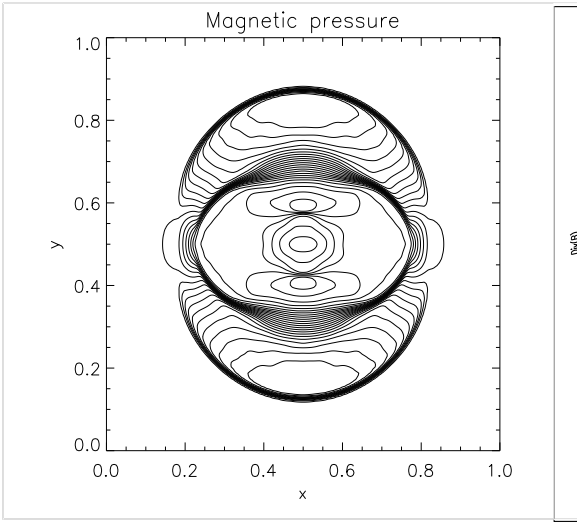
Magnetic pressure
1.0
0.8
0.6
0.4
0.2
0.0
y
0.0
0.2
0.4
0.6
0.8
1.0
x

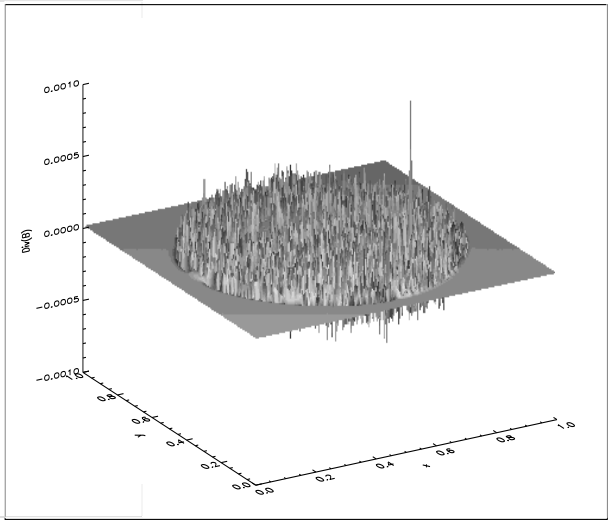
0.0010
0.0005
0.0000
−0.0005
−0.0010
Dw(B)
0.0
0.2
0.4
0.6
0.8
1.0
x
y

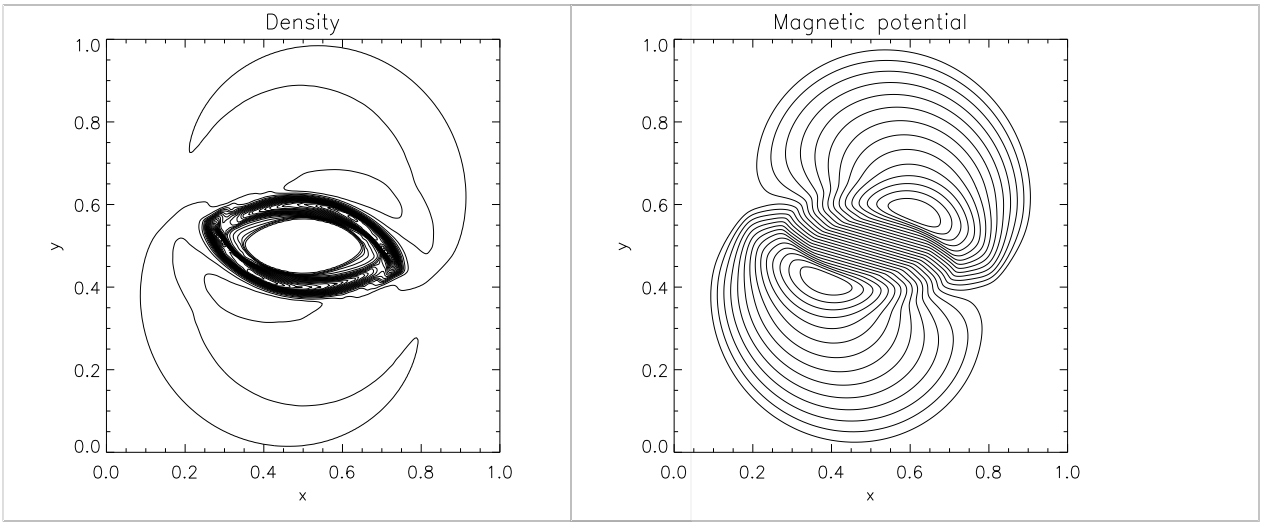
Density
Magnetic potential
Magnetic pressure
x
y
0.0
0.2
0.4
0.6
0.8
1.0

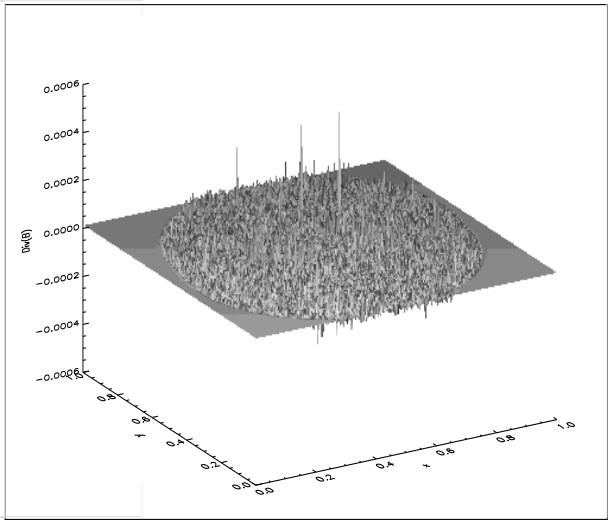
0.0006
0.0004
0.0002
0.0000
−0.0002
−0.0004
−0.0006
Dw(B)
x
y